Quarterly Technical Report

Growth, Characterization and Device Development in Monocrystalline Diamond Films

Supported under Grant #N00014-93-I-0437
Office of the Chief of Naval Research
Report for the period 4/1/96–6/30/96

R. F. Davis, R. J. Nemanich* and Z. Sitar
L. Bergman*, S. P. Bozeman, and M. T. McClure
North Carolina State University
c/o Materials Science and Engineering Department
*Department of Physics
Box 7907
Raleigh, NC 27695

June, 1996

REPORT DOCUMENTATION PAGE

Form Approved
OMB No. 0704-0188

1. AGENCY USE ONLY *(Leave blank)*

2. REPORT DATE
June, 1996

3. REPORT TYPE AND DATES COVERED
Quarterly Technical 4/1/96-6/30/96

4. TITLE AND SUBTITLE
Growth, Characterization and Device Development in Monocrystalline Diamond Films

5. FUNDING NUMBERS
s400003srr14
1114SS
N00179
N66005
4B855

6. AUTHOR(S)
R. F. Davis, R. J. Nemanich, and Z. Sitar

7. PERFORMING ORGANIZATION NAME(S) AND ADDRESS(ES)
North Carolina State University
Hillsborough Street
Raleigh, NC 27695

8. PERFORMING ORGANIZATION REPORT NUMBER
N00014-93-I-0437

9. SPONSORING/MONITORING AGENCY NAMES(S) AND ADDRESS(ES)
Sponsoring: ONR, Code 312, 800 N. Quincy, Arlington, VA 22217-5660
Monitoring: Admin. Contracting Officer, ONR, Regional Office Atlanta
101 Marietta Tower, Suite 2805
101 Marietta Street
Atlanta, GA 30323-0008

10. SPONSORING/MONITORING AGENCY REPORT NUMBER

11. SUPPLEMENTARY NOTES

12a. DISTRIBUTION/AVAILABILITY STATEMENT
Approved for Public Release; Distribution Unlimited

12b. DISTRIBUTION CODE

13. ABSTRACT *(Maximum 200 words)*

Nuclear transmutation of boron to lithium is being investigated for donor doping of diamond. Homoepitaxial ^{10}B enriched diamond films have been grown and characterized using Hall measurements and Raman and photoluminescence spectroscopies. The films have been neutron-irradiated at a dose of 3×10^{20} n/cm^2. Gamma ray spectroscopy of the samples indicates an activity of 5μCi of ^{110}Ag. The samples are now being cleaned to remove this contaminant. The field emission energy distribution was measured from a molybdenum nanoscale field emitter before and after diamond coating. After coating, the Mo needle had a lower "turn-on" voltage that was attributed to the diamond crystals acting as micro-tips which enhanced the field. The "turn-on" voltage further decreased after *in vacuo* annealing of this needle. A second peak appeared with an effective work function close to the expected value for molybdenum carbide. An attempt to hydrogen terminate the diamond coating was unsuccessful as the treatment removed the diamond coating and partially melted the needle. The increase in the "turn on" voltage most probably reflected the increase in the radius of curvature of the emission area. Under the conditions studied no peaks were observed that could be directly related to emission from the diamond particles. An in-depth review of the optical properties of diamond films and particles is also included.

14. SUBJECT TERMS
diamond, films, particles, doping, donor, nuclear transmutation, ^{10}B, Hall, photoluminescence, Raman spectroscopy, gamma ray spectroscopy, neutron-irradiation, field emission, energy distribution, molybdenum, molybdenum carbide, annealing, hydrogen termination, optical properties

15. NUMBER OF PAGES
64

16. PRICE CODE

17. SECURITY CLASSIFICATION OF REPORT	**18. SECURITY CLASSIFICATION OF THIS PAGE**	**19. SECURITY CLASSIFICATION OF ABSTRACT**	**20. LIMITATION OF ABSTRACT**
UNCLAS	UNCLAS	UNCLAS	SAR

NSN 7540-01-280-5500

Standard Form 298 (Rev. 2-89)
Prescribed by ANSI Std Z39-18
298-102

Table of Contents

I. Introduction

Diamond as a semiconductor in high-frequency, high-power transistors has unique advantages and disadvantages. Two advantages of diamond over other semiconductors used for these devices are its high thermal conductivity and high electric-field breakdown. The high thermal conductivity allows for higher power dissipation over similar devices made in Si or GaAs, and the higher electric field breakdown makes possible the production of substantially higher power, higher frequency devices than can be made with other commonly-used semiconductors.

In general, the use of bulk crystals severely limits the potential semiconductor applications of diamond. Among several problems typical for this approach are the difficulty of doping the bulk crystals, device integration problems, high cost and low area of such substrates. In principal, these problems can be alleviated via the availability of chemically vapor deposited (CVD) diamond films. Recent studies have shown that CVD diamond films have thermally activated conductivity with activation energies similar to crystalline diamonds with comparable doping levels. Acceptor doping via the gas phase is also possible during activated CVD growth by the addition of diborane to the primary gas stream.

The recently developed activated CVD methods have made feasible the growth of polycrystalline diamond thin films on many non-diamond substrates and the growth of single crystal thin films on diamond substrates. More specifically, single crystal epitaxial films have been grown on the {100} faces of natural and high pressure/high temperature synthetic crystals. Crystallographic perfection of these homoepitaxial films is comparable to that of natural diamond crystals. However, routes to the achievement of rapid nucleation on foreign substrates and heteroepitaxy on one or more of these substrates has proven more difficult to achieve. This area of study has been a principal focus of the research of this contract.

At present, the feasibility of diamond electronics has been demonstrated with several simple experimental devices, while the development of a true diamond-based semiconductor materials technology has several barriers which a host of investigators are struggling to surmount. It is in this latter regime of investigation that the research described in this report has and continues to address.

In this reporting period, (1) the status of the nuclear transmutation of boron to lithium as a means of donor doping diamond and (2) the field emission energy distribution of a non-hydrogenated and hydrogenated diamond-coated Mo needle are described. An in-depth review of the optical properties of diamond films and particles is also included. The following sections are self-contained in that they present an introduction, the experimental procedures, results and discussion, summary and indications of future research for the given research thrust.

II. Donor Doping of Diamond Using Nuclear Transmutation

A. Introduction

This report provides an update on an ongoing project at NCSU investigating Li incorporation into diamond via nuclear transmutation. This doping mechanism is of interest in diamond because of difficulties encountered in attempts to incorporate Li by more conventional means such as diffusion or incorporation during CVD. Additional background for this work has been described in previous quarterly reports.

Our approach has been to investigate transmutation in well characterized homoepitaxial films grown by established techniques. Growth and electrical measurements have been performed at Kobe Steel USA by researchers with extensive experience in electrical measurements on homoepitaxial and polycrystalline diamond film. Our isotopically-enriched boron source is diborane, one of the most common doping sources of boron for CVD diamond growth. The carrier concentration and mobility have been measured as a function of temperature prior to irradiation. The quality of the films and diamond substrates prior to irradiation has also been evaluated using Raman and photoluminescence spectroscopy. In addition, our experiments include control samples with no boron and with the natural abundance of boron to separate the effects of irradiation damage from the effects of Li production. Irradiation has been performed by Dr. S. Mirzadeh of the Nuclear Medicine group at Oak Ridge National Laboratory.

B. Experimental Procedure

Homoepitaxial boron doped films have been grown using microwave CVD with diborane as the dopant source. Table I shows the target boron concentrations for each of the five films. All films are grown on (100) oriented type 2a natural diamond substrates and range from 3 to 8 microns in thickness. The films were grown over a 3×3 mm^2 area on the 4×4 mm^2 substrates to isolate the films from the edges of the wafers. The isotopically enriched diborane is 96% ^{10}B and 4% ^{11}B. Films with the natural abundance of the two boron isotopes are included to aid in separating the effects of Li production from the effects of damage. The natural isotopic abundance of boron is 19% ^{10}B and 81% ^{11}B, so the maximum possible conversion of the natural abundance samples (#1 and #2) is 19%. Samples 4 and 5 have the same boron content to provide a duplicate experiment. In addition, measurements can be made of the back surfaces of the diamond wafers to analyze the effects of neutron irradiation on diamond which is free of boron. Metal contacts consisting of Ti and Au were applied. The carrier concentration and mobility were measured at several temperatures from 300 to 600 K using the Hall effect in a van der Pauw geometry.

Table I. Samples and Target Boron Content

Sample	Boron content (Target value, cm^{-3})	Isotopic Composition
1	10^{18}	natural abundance
2	10^{20}	natural abundance
3	10^{18}	^{10}B enriched
4	10^{20}	^{10}B enriched
5	10^{20}	^{10}B enriched

Raman and photoluminescence spectroscopy were used to provide a baseline measurement of the quality and defects in the films and substrates. It is expected that the films will be damaged during the irradiation process, so it is important to measure the quality of the films before irradiation. Raman measurements were made using the 5145Å line of an Argon laser, and photoluminescence measurements using the 4579Å line (2.71eV). The incident light was focused to a 10 µm spot size using a microscope, and the scattered light was analyzed using an ISA U-1000 scanning double monochromator.

Samples were irradiated by Dr. S. Mirzadeh of the Nuclear Medicine Group at Oak Ridge National Laboratory. The total dose was 9×10^{20}n/cm^2.

C. Results and Discussion

The diamond samples were irradiated at a dose of 9×10^{20} n/cm^2. The previously reported target dose of 3×10^{20} n/cm^2 was increased. Calculations performed by Dr. Mirzadeh indicate that this dose will convert 95% of the ^{10}B to ^{7}Li (Fig. 1).The samples exhibited a greater radioactivity than expected when removed from the reactor. As of 2/26/96, the package read 1 R/h unshielded and ~64 mR/h shielded with 1" lead. The samples were retested on 4/29/96 after removal from the packaging and a lower but still significant activity was detected. Gamma ray spectroscopy indicated that the remaining activity consisted of approximately 5µCi of ^{110}Ag. The samples have now been returned to NCSU, where they will be cleaned to remove the remaining silver.

D. Conclusions

In summary, nuclear transmutation is being investigated as a means for donor doping of diamond. To date samples have been prepared for irradiation, baseline electrical measurements and optical measurements have been performed, and samples have been irradiated at a dose of 9×10^{20}n/cm^2.

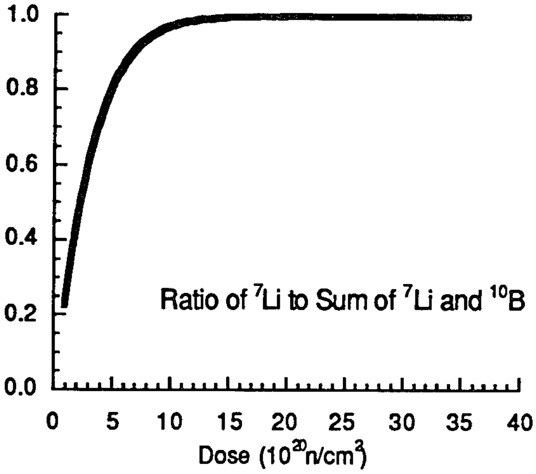

Figure 1. Percentage of ^{10}B converted to ^{7}Li as a function of neutron dose.

E. Future Research Plans and Goals

Following cleaning of the samples, post irradiation studies will begin with optical assessment of the damage via Raman and photoluminescence spectroscopy. We will then attempt to remove the damage via annealing. If the damage can be recovered, additional Hall measurements will be performed.

III. Spectral Analysis of Field Emitted Electrons from Diamond-Coated Nanoscale Molybdenum Emitters

A. Introduction

For several years, the study of field emitters has been of interest as the possibility of flat panel displays and vacuum microelectronics has appeared feasible [1]. One drawback to traditional field emitter materials, Si and Mo, has been contamination of surface and surface degradation through back sputtering by the ambient ions. One approach to counteract these drawbacks has been coating the emitters with diamond to protect the surface from oxidation and ion bombardment. Diamond has an additional attraction of negative electron affinity under certain conditions [2]. However, traditional Fowler-Nordheim analysis of I-V measurements is not well suited for curved surfaces and low work function materials [3, 4]. On the other hand, field emission energy distribution analysis of the emitted electrons is ideally suited for the detection of materials with a negative electron affinity and would reveal any other effects a diamond coating would have on the emitter. Also, this analysis technique would indicate the energy relationship between the applied voltage and the emitted electrons.

This report relates the experimental results measuring the field emission energy distribution of a diamond coated Mo emitter. The data was compared to the same Mo emitter before coating and several *in vacuo* thermal treatments were performed to determine their effects on electron emission. The analyzer used was a hemispherical energy analyzer typically used for x-ray photoelectron spectroscopy or Auger electron spectroscopy.

B. Experimental Approach

Mo Needle Preparation and Diamond Powder Coating. A single emitter tip was made from 99.95% pure Mo wire with a diameter of 0.125mm. The wire was held in a Cu tube and then electrochemically etched in a concentrated KOH solution. This technique has consistently produced needles with a radius of curvature approximately 500 µm.

After the initial data was collected, the needle was coated with diamond powder via a dielectrophoresis method. The diamond powder (size range: 0-0.25 µm) was suspended in a ethanol solution and voltage was applied between the Mo needle and the container. The non-uniform field generated by the needle created an impelling force driving the diamond particles toward the region of highest field (i.e. the tip end). SEM observation after coating revealed the entire tip end was covered by diamond powder.

Testing Configuration. The Mo needle was set into the holder and centered within a circular gate where the needle was the "cold cathode" and the gate was the "extraction grid." The gate was electrically grounded and had a 500 µm opening and a tip-to-gate separation distance of 400 µm. A negative voltage was applied to the tip, see Fig. 1. The energy analyzer used was a CLAM II hemispherical energy analyzer from Vacuum Generators, Ltd., typically used in x-ray photoelectron spectroscopy or Auger electron spectroscopy. Both the gate and analyzer were at the same ground potential. Typical data collection conditions included a dwell time of 100 ms, an energy step of 0.025 eV, and 3 scans were taken over the desired energy range.

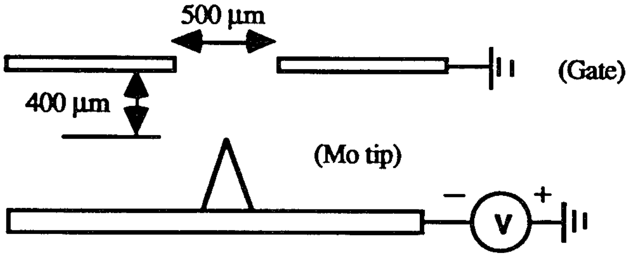

Figure 1. Schematic drawing of sample holder and voltage connections.

Experimental Procedure. After the sample was placed into the vacuum chamber, an initial thermal desorption treatment was performed. The sample holder was heated to 500°C for 1 hour and the chamber pressure was in the 10^{-7} Torr range. All emission data was collected under UHV conditions (typically 10^{-9} Torr). Next, the sample was removed from the chamber and coated with diamond powder via the dielectrophoresis method. To remove any atmospheric contaminants and desorb any solvent, the sample holder was heated *in vacuo* to 400°C for 3 hours before taking any measurements. Next, a thermal annealing treatment was performed by heating *in vacuo* to 600°C for 90 minutes. For the final heat treatment, the sample was transferred to a microwave plasma diamond CVD system (ASTeX, Inc.) for the H_2 plasma treatment. The sample was heated to 620°C for 30 minutes downstream from the plasma, then the sample was transferred back to the analysis chamber and data was collected. After this series, the sample was imaged in a scanning electron microscope.

C. Results

Table I summarizes the observed energy shift between the applied voltage and the peak maximum and the voltage for which there was perceptible signal (i. e. count rates > $10s^{-1}$), hereafter termed "turn-on" voltage. Figure 2 displays spectra of similar count rate for the different treatments. The spectra typically had a rapid increase on the high energy side of the peak and a less rapid decay on the lower energy side of the peak. The "turn-on" voltage for the bare Mo needle was -450 V. After diamond coating the "turn-on" voltage decreased to -350 V and it decreased to -280 V after annealing the diamond coated needle. The "turn-on" voltage increased to -650 V after attempting to hydrogen terminate the diamond coating.

The energy difference between the applied voltage and the peak maximum for the Mo tip was -4.1 eV for all voltages and the peak FWHM was 0.7±0.1 eV. After diamond coating, the energy difference increased to -5.4eV for the "turn-on" voltage and increased with applied voltage to -11 eV for -525 V with a FWHM of 0.7±0.1 eV. Two peaks appeared after annealing the diamond coated needle at an energy difference of -4.6 eV and -3.4 eV. The second peak appeared only above voltages of -400 V. The peak FWHM for both peaks was 0.8±01 eV. After attempting to hydrogen terminate the diamond coating, only one peak was observed and the energy difference was -3.4 eV with a FWHM of 0.7±0.1 eV.

SEM micrographs taken after the H_2 plasma treatment revealed that the diamond powder coating near the tip of the needle had been removed. The tip had partially melted and bent away from the gate.

Table I. Summary Table of Energy Separation Between the Applied Voltage and Emission Peak and "Turn-on" Voltages for the Different Treatments

Treatment	Energy Shift (eV)	"Turn-on" Voltage (V)
bare Mo	-4.1	-450
Diamond coated Mo	-5.4 to -11 increased with voltage	-350
Diamond coated Mo - annealed	-4.6 and -3.4	-280
Diamond coated Mo - H_2 plasma	-3.4	-650

D. Discussion

The energy difference between the applied voltage and the peak maximum for different treatments is summarized in Table I. For the uncoated Mo needle, the peak maximum was observed to be 4.25±0.25 eV below the applied voltage, which is in agreement with the reported effective work function for Mo (4.2-4.4 eV) [1]. While no reported values for molybdenum carbide could be found, the following trends were noted. TiC had an effective work function 0.7 eV less than Ti and TaC had an effective work function 0.9 eV less than Ta. Since the refractory metals share many common attributes, it is reasonable to assume that the effective work function of molybdenum carbide is lower than that of Mo [1]. Therefore, the peaks recorded that were around 3.4 eV below the applied voltage may be attributed to emission from the carbide phase, while the peaks approximately 4.25±0.25 eV below the applied voltage can be attributed to emission from Mo. However, the presence of Mo_xC cannot be confirmed until further analysis of the needle is done. The reported work function values for diamond are either 1.0 eV or negative electron affinity depending on surface termination. No peaks were observed corresponding to those values.

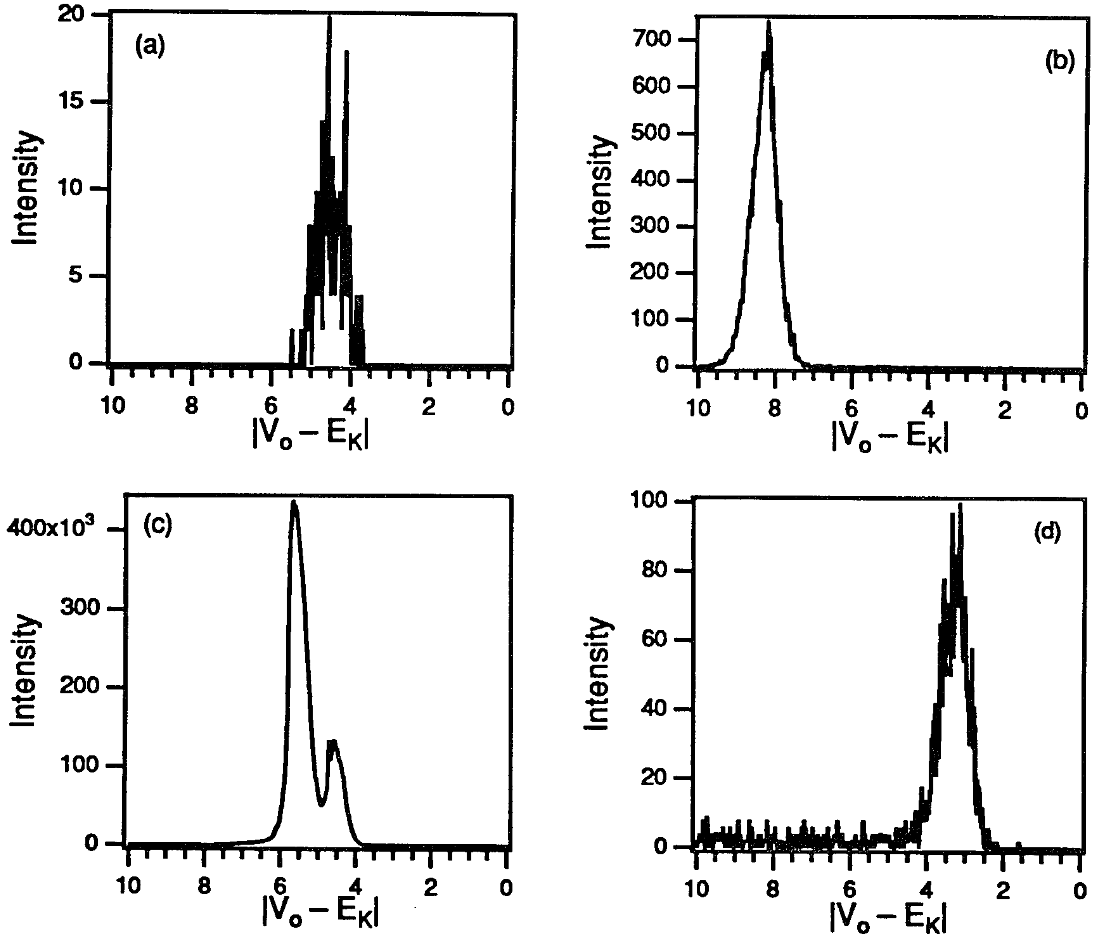

Figure 2. Typical energy distribution spectra for the (a) Mo needle (-450 V), (b) after diamond coating (-450 V), (c) after annealing (-450 V), and (d) after H_2 plasma treatment (-700 V).

The decrease in "turn-on" voltage after coating the Mo needle with diamond powder probably resulted in a change in the field distribution to enhance emission; however, the large work functions observed suggest that the emission did not emanate from the diamond coating. After annealing the diamond coated Mo needle, the morphology of the coating may have changed and modified the field distribution at the emitting area. SEM micrographs after the H_2 plasma treatment revealed that the tip was no longer covered with diamond and the needle had bent. The increase in radius of curvature caused an increase in the "turn-on" voltage.

After those treatments that resulted in the formation of a carbide phase, it would be reasonable to assume that the lower work function areas would begin to emit at lower voltages. This supposition is counter to what was observed. One possible explanation is that the carbide phase formed only where there was significant contact between the Mo needle and diamond crystals. It is unlikely that the entire crystal was consumed in the formation of the carbide, therefore, the remaining diamond crystal would have been a scattering barrier to electrons emitted from the carbide phase. At higher voltages, where emission appeared to have come from the carbide phase, the voltage may have been sufficient to cause ballistic transport of electrons from the carbide through the obstructing diamond particle.

E. Conclusions

The field emission energy distribution was successfully measured from a diamond powder coated, nanoscale Mo needle, after several thermal treatments, using a hemispherical energy analyzer. Examination of the field emission energy distribution (FEED) spectra yielded valuable information not gained during standard I-V measurements. Measuring the energy difference between the applied voltage and the field emission peak provided information regarding the work function of the emission area. The variation in this energy difference for the diamond coated Mo needle indicated that diamond did not emit under the conditions investigated. The FEED spectra also indicated that both Mo and possibly Mo_xC regions emitted after annealing the diamond powder coated needle.

F. Future Research Plans and Goals

These initial experiments revealed that the energy distribution of field emission electrons provided important information not obtained in I-V measurements. Several questions were also raised. For instance, although Mo_xC probably has a lower work function than Mo a higher voltage was required to induce emission from these regions. To determine whether the lower work function of diamond is of relevance, or whether the lowering of the "turn-on" voltage is exclusively due to topographic effects leading to further field enhancements, graphite coated needles will be investigated. Comparison experiments between Mo and Si needles will also be performed to investigate the differences in these two commonly used emitter materials.

G. References

1. S. Iannazzo, Solid State Electronics **36** (3), 301-20 (1993).
2. J. van der Weide and R. J. Nemanich, Applied Physics Letters **62** (16), 1878-80 (1993).
3. D. Nicolaescu, J. Vac. Sci. Technol. **B 11** (2), 392-395 (1993).
4. R. H. Fowler and L. W. Nordheim, Proc. R. Soc. London Ser. **A 119**, 173 (1928).

IV. Optical Properties of Diamond Films and Particles

Leah Bergman and Robert J. Nemanich

Department of Physics and Department of Materials Science and Engineering,
North Carolina State University, Raleigh, North Carolina 27695-8202, USA

Reviewed by Alan T. Collins, King's College London, UK

1. Introduction

The unique properties of diamond such as hardness, UV optical transparency, high thermal conductivity and its semiconducting behavior have led to the extensive development of new growth methods and to innovative research in the field of diamond devices and applications [1-3]. Diamond films differ in many ways from natural diamond crystals due to the synthetic method of growth, in particular having their own characteristic defects and impurities [3]. In order to achieve the goal of producing diamond films of sufficiently high quality to be viable as high performance semiconductor devices, it is crucial to gain knowledge of the characteristic impurity and defect states.

There are various methods of characterizing semiconductor materials that in general can be categorized as surface, imaging and bulk analysis techniques [4]. Surface analysis techniques include Auger and Photoelectron Spectroscopy. Imaging analysis techniques consist of scanning electron microscopy (SEM) and transmission electron microscopy (TEM), while the bulk analysis techniques are cathodoluminescence (CL), photoluminescence (PL) and Raman spectroscopy. The latter two spectroscopy techniques have been proven useful in analyzing crystalline diamond and, more recently, diamond films [5-10]. Raman and PL, moreover, are non-destructive methods of spectroscopy that can be applied to a wide range of diamond characterizations and analyses.

Important applications of Raman spectroscopy to diamond films are the identification of the diamond structure and the amorphous structure of carbon (graphitic phase) that coexist in many of the diamond films [8, 9], and obtaining a quantitative measure of the stress in the film and analyzing its possible sources [11-15]. The analysis of PL spectra, on the other hand, can be used to provide information about the impurities and defects that are present in the diamond film and may give an insight to the mechanism of impurity incorporation and doping [12, 15, 16]. These two complementary optical techniques can provide crucial initial insight into the diamond film quality.

To be published in Handbook of Optical Properties, *Vol. II. Optics of Small Particles, Interfaces and Surfaces, Editors: R. E. Hummel and P. Wibmann, CRC Press 1996.*

This chapter presents a review of investigations into the structure, substrate-film interface and impurities of diamond thin films grown on silicon substrates utilizing Raman and photoluminescence spectroscopy. The remainder of this chapter is organized as follows. In Section 2 the background theory of Raman scattering and PL is presented. The issue of the graphitic phase, as a defect in diamond film, is discussed in Section 3. Lastly, Sections 4 and 5 focus on the nitrogen and silicon impurities in diamond films, respectively.

2. Raman Scattering and Photoluminescence: General Aspects

The Raman effect in solids [17-23] is an inelastic scattering of the incident photons by the crystal electrons distributed around the lattice nuclei. In the photon-electron interaction, the incoming photons exchange a quantum of energy with the electrons via the creation or annihilation of lattice vibrations (phonons). As a result, the scattered photons lose or gain an energy quantum depending on whether a phonon was created (Stokes process) or annihilated (Anti-Stokes process). In Raman spectroscopy, the energy of the scattered photons is measured; thus a characteristic value of the vibration energy of a specific material may be obtained.

Figure 2.1 illustrates the Raman scattering process. The sample is irradiated by a monochromatic laser beam of frequency ν_i chosen to be in the visible region. The incident photons create or annihilate crystal vibrations of frequency ν_p and the observed scattered beam consists of light of frequency ν_i-ν_p and ν_i+ν_p due to the Stokes and Anti-Stokes mechanisms respectively. The scattered beam has an additional light component of the same frequency as the incident light (ν_i) that arises from the elastic Rayleigh scattering. A typical Raman spectrum of a crystal exhibits sharp bands at frequencies $\pm\nu_p$ which are measured as a shift, called the Raman Shift, from the incident beam frequency ν_i.

The spectral unit of the wavenumber, cm^{-1}, is conventionally employed in Raman spectroscopy. The wavenumber $\tilde{\nu}$ is defined by

$$\tilde{\nu} = \frac{\nu}{c} = \frac{1}{\lambda}\mathrm{cm}^{-1} \tag{2.1}$$

where c is the velocity of light (3×10^{10} cm/s), ν is the frequency of the scattered light in units of 1/s (Hz), and λ is the wavelength in units of cm.

The classical theory of the Raman effect treats the light scattering event in terms of an oscillating dipole [24-26]. In a material of polarizability tensor α, the induced dipole moment, **p**, is given by

$$\mathbf{p} = \alpha\mathbf{E} \tag{2.2}$$

where **E** is due to the oscillating incident electric field of a monochromatic source (laser) of frequency ν_i represented by

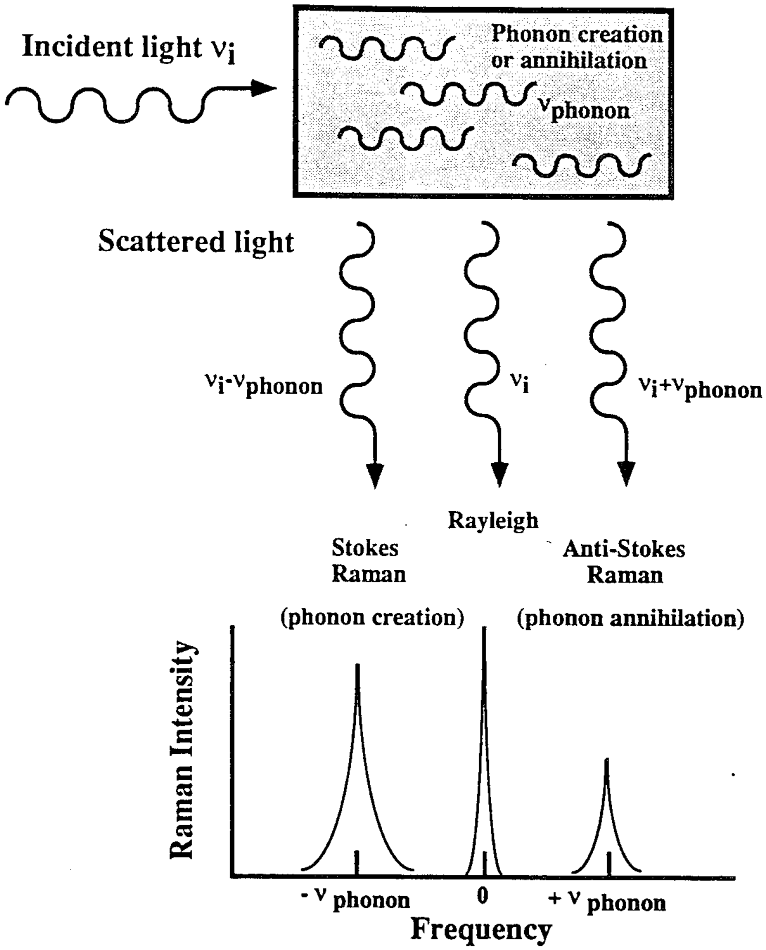

Figure 2.1 Schematic representation of the Raman scattering effect in a solid and the resulting Raman spectrum of the Stokes and the Anti-Stokes bands.

$$\mathbf{E} = \mathbf{E_0} \cos(2\pi\nu_i t). \tag{2.3}$$

The vibrational modes of a solid are also of an oscillating nature that can be described by the normal coordinate of the vibrations, Q:

$$Q = Q_0 \cos(2\pi \nu_p t). \tag{2.4}$$

The oscillation presented in Eq. 2.4 may affect the polarizability of the material; this effect for small vibrational amplitude can be expressed as

$$\alpha = \alpha_0 + \left(\frac{\partial\alpha}{\partial Q}\right)_0 Q + \text{ higher - order terms.} \tag{2.5}$$

Substituting Eqs. 2.3 to 2.5 into Eq. 2.2 yields what is known as the Raman scattering equation:

$$\mathbf{p} = \alpha_0 \mathbf{E}_0 \cos(2\pi\nu_i) + \frac{1}{2}\mathbf{E}_0 Q_0 \left(\frac{\partial\alpha}{\partial Q}\right)_0 \left[\cos\{2\pi(\nu_i + \nu_p)t\} + \cos\{2\pi(\nu_i - \nu_p)t\}\right]. \quad (2.6)$$

The first term in Eq. 2.6 represents an oscillating dipole that radiates light of frequency ν_i corresponding to the elastic Rayleigh scattering, while the other two terms correspond to the Raman inelastic scattering process of frequencies $\nu_i \pm \nu_p$ (anti-Stokes and Stokes). When the polarizability is independent of a change of the normal coordinates, i.e.

$$\left(\frac{\partial\alpha}{\partial Q}\right) = 0,$$

the vibration of frequency ν_p is not Raman active.

Equation 2.2 has important practical applications to determining the phonon symmetry in a given material. Since the polarizability α (a symmetric 3×3 tensor) exhibits the same symmetry as the phonon vibrations, and the polarization states of the incident ($\mathbf{E}_0$) and scattered ($\mathbf{p}$) light can experimentally be measured, the components of α can readily be determined.

One of the most important aspects of Raman scattering in solids arises from conservation of energy and wavevector, as described by the conservation laws:

$$h\nu_{\text{scattering}} = h\nu_i \pm h\nu_p \quad (2.7a)$$

for energy conservation, and

$$\mathbf{k}_{\text{scattering}} = \mathbf{k}_i \pm \mathbf{k}_p \quad (2.7b)$$

for conservation of the wavevector $\mathbf{k}_p$ of the crystal momentum, where the phonon energy and wavevector are related via the dispersion relation of the material. In a material consisting of a long range periodic lattice, all of the vibrational modes can be described with a well defined $\mathbf{k}_p$; the above conservation laws thus hold, and the Raman spectrum exhibits a sharp band at the characteristic ν_p. The resulting Raman lineshape can be described as a Lorentzian function of a parameter Γ that specifies the natural linewidth of the function [27, 28]. The physical interpretation of the natural linewidth may be derived from the uncertainty principle,

$$\tau\Delta E = h/2\pi, \quad (2.8)$$

where ΔE is taken to be the linewidth Γ (in units of energy) and τ is the characteristic phonon lifetime. In a high quality diamond crystal the natural Raman linewidth is determined by the time it takes the optical phonon to decay into the acoustical phonons [28]. Any value of linewidth which is larger than the one expected from a good quality crystal implies the existence of lifetime shortening mechanisms in the material.

If the material does not exhibit long range order, the vibrational modes cannot be described with a single charcteristic $\mathbf{k}_p$ (as expressed in Eq. 2.7). Each individual mode may be represented by a distribution of phonon wavevectors. Thus all modes with wavevector components that satisfy the scattering relations will be observed. The Raman spectrum in this case is very broad and often reflects the phonon-density of states of the material. Another broadening mechanism which may affect the Raman lineshape arises from the confinement of the phonons in small domains [29]. The domain size, d, is related to the phonon wavevector, k, via the uncertainty relation $\Delta k \sim 2\pi/d$; thus the domain size determines the range of the wavevectors that are allowed to participate in the Raman process. The resulting Raman lineshape reflects the dispersion relation for a given material.

As opposed to the Raman process, where the light scatters through interaction with the continuum of the crystal vibrations, photoluminescence is due to a radiative recombination mechanism [27, 30-32]. The most common origins of photoluminescence are from recombination of carriers at or near the band edge or from defect or impurity centers within the band gap. The optically active defect and impurity centers, termed optical centers, can often be excited with both above-bandgap and sub-bandgap light. Radiative recombination is one way an optical center returns to its equilibrium state after being perturbed by the excitation.

The basic mechanism of the PL process is presented in Fig. 2.2. In the figure, process **1** indicates the absorption of light by an optical center which results in the up-transition of the optical center into its excited state. Process **2** is the spontaneous emission of a quantum of light by the optical center in order to reach the ground state. These two processes are the most common ones that an optical center may undergo. A less common route to the ground state is the induced emission which requires a quantum of radiation (light) to be absorbed by the optical center in its excited state in order to undergo the transition, shown by process **3** in the figure.

The dynamics of the transitions are determined by the recombination mechanisms that the optical systems undergo, and can be described as probabilistic events [33]. Let N_G and N_E be the concentrations of the optical systems in the ground and excited state respectively. Then the rate of change of population N_E due to the absorption is

$$dN_E/dt = N_G B_1 \rho(\tilde{\nu}) \tag{2.9}$$

where $\rho(\tilde{\nu}) \sim (\tilde{\nu})^3/(\exp(hc\tilde{\nu}/kT)-1)$ is the spectral radiation density and $\tilde{\nu}$ is the wavenumber. The constant B_1 is the Einstein coefficient which is directly related, as will be explained in the next paragraph, to the coupling process of the light with the optical center. Similarly, the rate of change of N_E due to the induced emission is given by

$$dN_E/dt = -N_E B_1 \rho(\tilde{\nu}), \tag{2.10}$$

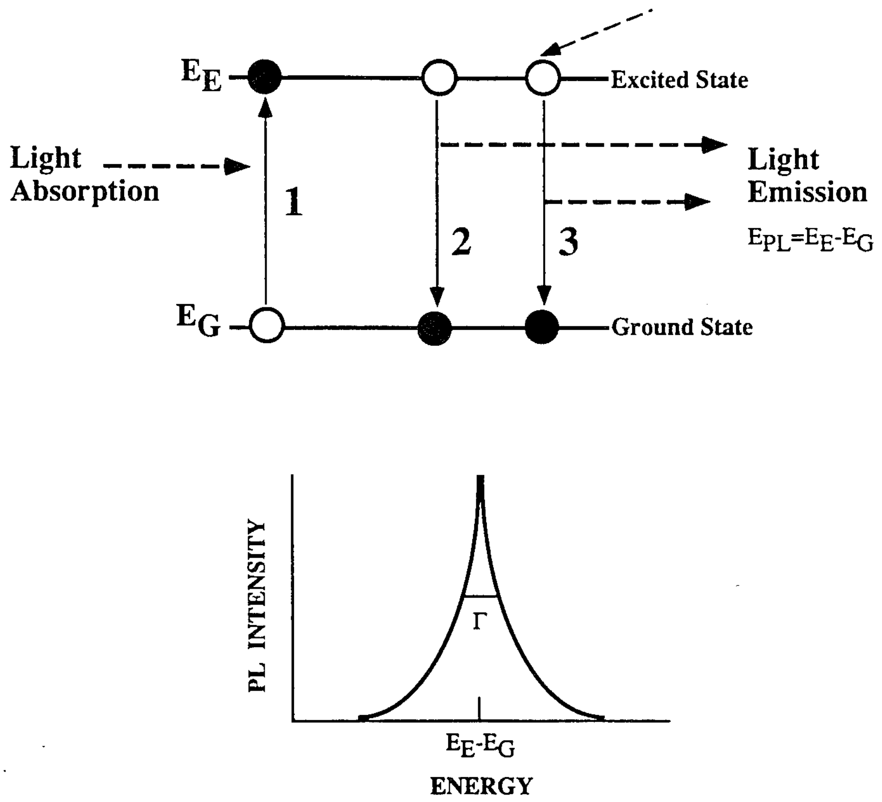

Figure 2.2 The photoluminescence process in an optical center involves an excitation via light absorption and a recombination mechanism along with light emission.

and for the spontaneous emission,

$$dN_E/dt = -N_E B_2, \tag{2.11}$$

were B_2 is the Einstein coefficient for this process. Upon shining a light source on the optical systems all of the above processes are initiated concurrently, and the net rate of population change can be analytically described by

$$dN_E/dt = N_G B_1 \rho(\tilde{\nu}) - N_E B_1 \rho(\tilde{\nu}) - N_E B_2. \tag{2.12}$$

When no non-radiative channels are present, the population change as expressed in Equation 2.12 is proportional to the luminescence intensity. From the thermal equilibrium conditions $dN_E/dt=0$ and $N_E/N_G \sim \exp\{-(E_E-E_G)/kT)\}$ the relation $B_2 \sim \tilde{\nu}^3 B_1$ between the Einstein coefficients is obtained.

The physics of luminescence, which specifically concerns the interaction of the light with the optical center, is conveyed in the Einstein coefficients. The absorbed light induces an electric dipole moment μ in the optical center which couples the ground state Ψ_G to the excited state Ψ_E. The transition probability $|R|^2$ analytically describes this process:

$$|R|^2 = \left|\int \psi_E^* \mu \psi_G \, d\tau\right|^2 \propto B_i \tag{2.13}$$

The transition probability function (and thus the Einstein coefficients B_i) determines the selection rules of a transition: it is zero for a forbidden transition and non-zero for an allowed transition. Furthermore, when spontaneous emission is the only channel of decay to the ground state, the lifetime of the transition is inversely proportional to B_2.

In the above discussion the physical system of the states E_G and E_E in Fig. 2.2 was not specified. Various photoluminescence mechanisms in semiconductors may arise depending on the exact physical system. For example, in semiconductor materials these two energy states can be associated with the acceptor and donor levels which lie in the bandgap of the material. Upon an electron transition from the donor level to the acceptor level a quantum of energy may be dissipated into light and give rise to luminescence. The energy released via the donor-acceptor transitions can be expressed as a Coulomb interaction of the form: $E(r) = E_G - (E_D + E_A) + B/r$ where E_G, E_D and E_A are the gap, donor and acceptor ionisation energies respectively, r is the separation of the donor and the acceptor in the matrix, and B is a constant. Figure 2.3 (a-d) schematically represent four possible routes for luminescence to occur. As in Raman scattering, the resulting lineshape of the PL process in a high quality crystalline material is a Lorentzian the width of which is in this case related to the lifetime of the transition.

3. The Diamond and Graphitic Phase in Diamond Films

3.1. Diamond and Graphitic Bonding in Carbon Films

Carbon films produced by vapor deposition techniques have been characterized as diamond [34-36] or diamond-like [37-40]. The difference between the two categories lies in the types of atomic bonding configurations that the carbon atoms possess as a result of the growth conditions.

Raman spectroscopy has been used to investigate the various bonding configurations in the carbon films and to classify the composite nature found in a given film [8]. The latter is of great interest in semiconductor applications since the various types of microstructures and carbon forms in a particular film may be a controlling factor in electronic transport as well as in the electronic emission properties. According to this work the carbon films can be in four different possible forms (that may coexist in a given film as a composite): sp^3-carbon in either amorphous or crystalline (diamond) form, and sp^2-carbon also in either amorphous or crystalline (graphite) structures. In the study four possible types of carbon bonding were investigated; in addition, the influence of possible structures on the spectra was analyzed and in light of the results the bonding types in diamond and diamond-like films were identified. The following presents a more detailed review of the Raman investigations carried out in these studies [8]. Related studies which have supported these findings have been reported by Hyer *et al.*, Knight *et al.*, and Kobashi *et al.* [41-43].

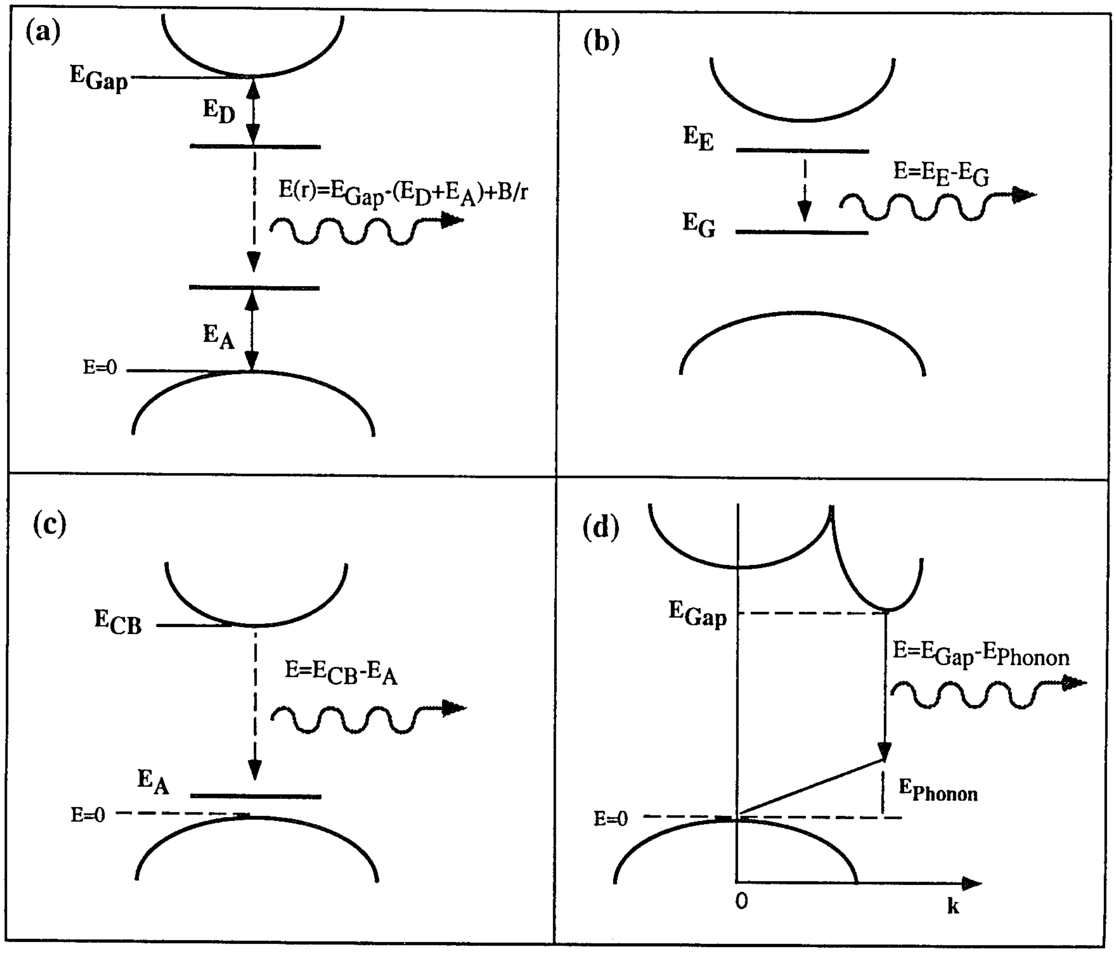

Figure 2.3 Various photoluminescence mechanisms due to: (a) donor-acceptor recombination, (b) transition between impurity energy levels, (c) conduction band and acceptor (or impurity) transition, (d) conduction to valence band indirect recombination.

The first and second order Raman spectra of diamond crystal [44] and graphite crystal [45] are compared in Fig. 3.1 (a-b). The sharp features at 1332 and 1580 cm^{-1} are the first order modes of diamond and graphite crystals, respectively. These frequencies are indicative of the different bond strengths for which the graphite bonding is the strongest of the two. The bonding in graphite exhibits one of the largest anisotropies of any solid. The nearest-neighbor C-C bonding in graphite is considerably stronger than the C-C bond in diamond [46]. In contrast, the bonding between the graphite planes is very weak and exhibits a Van der Waals character [46]. The very weak and very strong bonding in graphite yields both unusually low (42 cm^{-1}) and high (1580 cm^{-1}) frequency contributions to the lattice vibration spectrum [45]. The second order Raman feature is due to the scattering mechanism which involves two phonons with opposite crystal momentum vectors of nearly equal magnitudes. A detailed investigation of the second order Raman scattering of crystalline and micro-crystalline graphite is presented in [45].

Samples considered to be amorphous sp^2-carbon have been reported by Solin *et al.* [47]. The spectra (labeled α) of the film, overlaid with that of the crystalline graphite, is shown in Fig. 3.1b. The spectra of amorphous films consisting of pure disordered sp^3-carbon structure have not been reported and the Raman spectra of such material could only be speculated to be similar to amorphous silicon. This is a reasonable approximation since amorphous silicon consists of a disordered state of tetrahedral sp^3-type bonding. The inferred spectra of amorphous sp^3-carbon is shown in Fig. 3.1a.

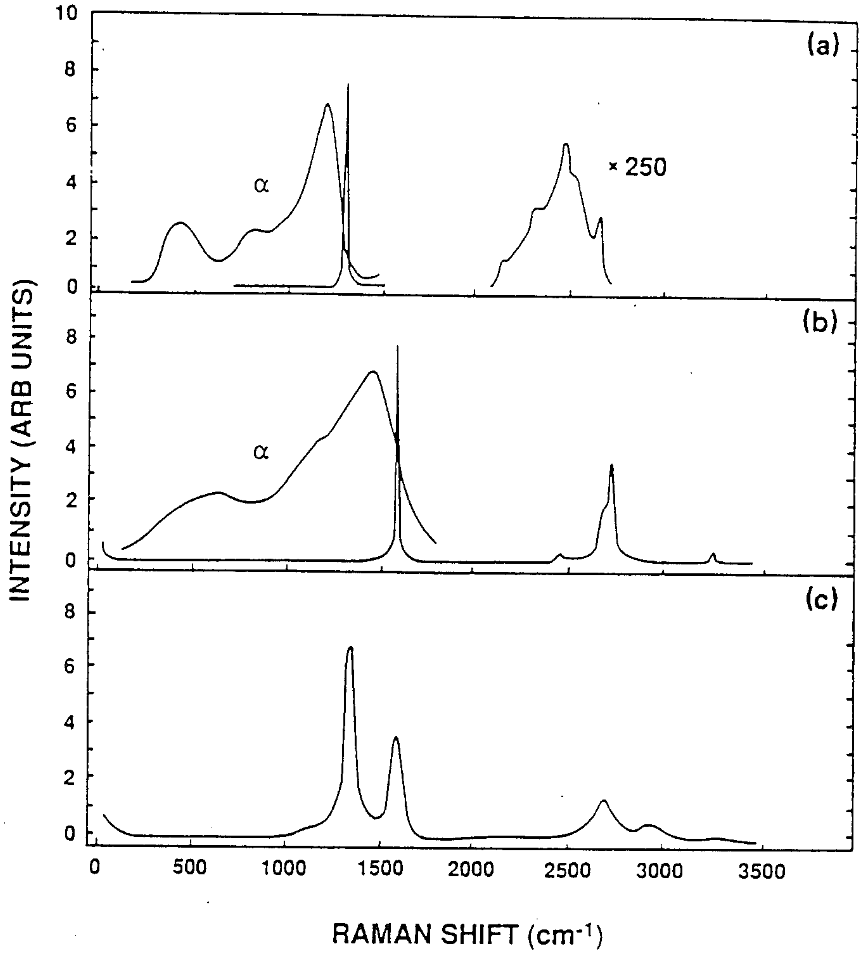

Figure 3.1 The Raman spectra of (a) diamond, (b) graphite, and (c) microcrystalline graphite. The solid lines in (a) and (b) represent the first-and second-order spectra of crystalline diamond and graphite, respectively. The line in (a) labeled α is the spectrum of a-Si scaled to the diamond frequency to represent the spectrum of amorphous sp^3-carbon, while the line in (b) labeled α is that due to amorphous sp^2-carbon. From Nemanich *et al.* [8].

3.1.1. Composite Properties

It has been suggested that three different composite structures might exist in the carbon films: the micron-scale, the microcrystalline, and the atomically disordered network. The characteristics of the Raman scattering from each structure have been investigated in [8]. The following discussion outlines some aspects of the structural properties of the films and the related vibrational excitations.

Micron-scale composite is defined as a film consisting of ~ 1 μm domains of diamond as well as of graphite. The decay length of the phonons is in general < 1 μm; therefore boundary scattering will not significantly affect the phonon lifetime. This means that the vibrational excitations exhibit the same spectral response as the bulk materials, i.e. the same Raman frequencies. However, the optical properties of graphite (which is absorbing material) and of diamond (which is transparent material) are different and as such will affect the Raman scattering intensities. In general, the Raman cross section and hence the intensity of absorbing materials is enhanced due to the resonance effects. It has previously been reported that the cross section of the 1580 cm^{-1} mode of graphite is ~ 75 times larger than that of diamond when normalized for carbon sites [48]. Thus, Raman scattering from similar volumes of graphite and diamond will emphasize the graphite structure.

Microcrystalline (or nanocrystalline) samples can exhibit domains of various sizes which are usually much less than 1 μm; the domains that are in this nano-meter scale have a strong effect on the Raman scattering, as is discussed next. The phonon decay length is often larger than the domain size dimension; thus the boundary scattering causes the vibrational excitations to exhibit life-time broadened peak widths. In addition, from the Heisenberg uncertainty principle, the wave vector of the excitation is uncertain ($\Delta k \sim 2\pi/d$, where d is the domain size), and the momentum selection rules of the Raman process are relaxed [29]. The domain size effects are pronounced on microcrystalline graphite as is shown in Fig. 3.1c. The Raman lines of the microcrystalline graphite exhibit broader peaks than those of the crystalline graphite. Furthermore, a new band in the first-order spectrum can be observed at 1355 cm^{-1} which is attributed to the uncertainty of the wave vector of the vibrations due to the finite size of the domains. An additional band can also be observed at 2940 cm^{-1} in the second-order spectrum. As in the micron-scale composite, the Raman cross section of the graphite component in the microcrystalline domain is ~ 75 larger than that of diamond.

The last structure to be considered is the atomically disordered (amorphous) network. In the case of carbon material, the amorphous network may possibly be composed of sp^2 and sp^3 bonding [49]. The vibrational excitations would not be confined to a single atomic site, and thus would represent an average of the network possibilities. The optical properties would not strongly favor enhancement of the sp^2 over the sp^3 bonding, and the Raman cross sections are speculated to be similar. The anticipated Raman spectrum should be very broad extending from ~1100 to 1600 cm^{-1}. Extensive studies on amorphous carbon networks have been conducted and are ongoing [49-51], but at present there is yet to be achieved a complete understanding of its complex nature.

3.1.2. Diamond and Diamond-like Films

Lastly, the properties of diamond-like and diamond film have also been investigated [8]. The Raman spectra of two diamond-like films produced under different deposition conditions are shown in Fig. 3.2. The spectra presented in the figure are not similar to any of the spectra previously discussed as characteristic of amorphous or crystalline sp^2-carbon or sp^3-carbon (see Fig. 3.1a-b). Although the 1590 cm^{-1} band can be attributed to graphite, the 1355 cm^{-1} band has no apparent origin.

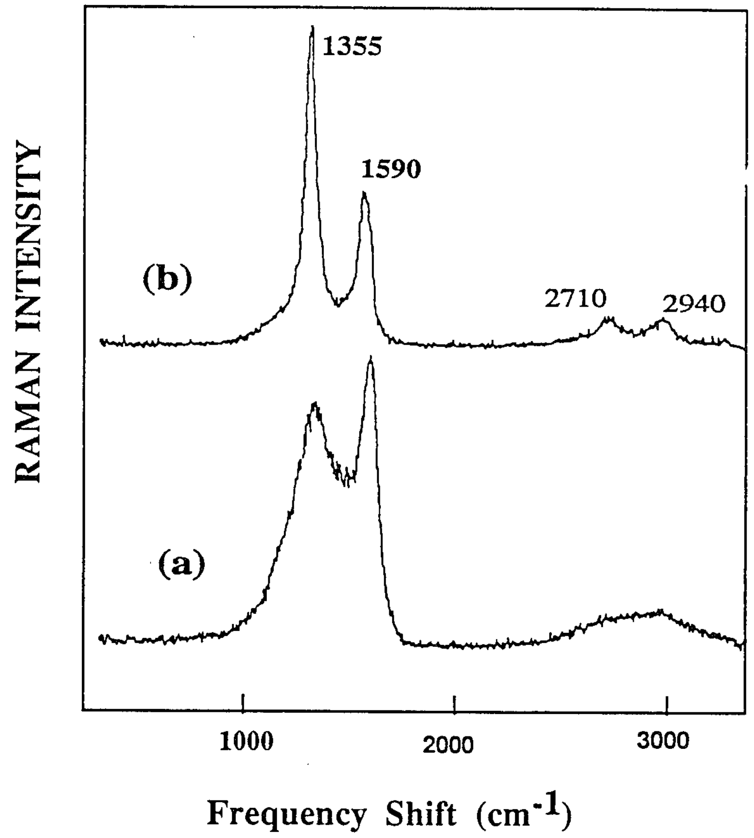

Figure 3.2 The Raman spectra of diamondlike films produced with different deposition conditions. Both spectra exhibit the 1355 and the 1590 cm^{-1} bands attributed to the disordered and to the ordered mode of graphite respectively. From Nemanich *et al.* [8].

One argument against the assignment of the 1355 cm^{-1} line to diamond is that its frequency is higher than any of the vibration frequencies of the diamond lattice. While effects such as strain are known to shift frequencies to a higher wavelength, the observed large shift would indicate an infeasible compressive stress of ~12 GPa. The other argument that this peak is most likely not due to the diamond structure is based on the interpretation of the second-order spectrum of graphite and the spectrum of microcrystalline graphite samples. The strongest band in the second-order spectrum of crystalline graphite is at 2710 cm^{-1} which is also present in the spectra of the diamond-like films. This band at twice the frequency of 1355 cm^{-1} indicates that it is a first order Raman band related to graphite. Since the 1355 cm^{-1} band is also observed in the spectrum of the microcrystalline graphite (due to small domain size activation), it may be concluded that the 1355 cm^{-1} band in the diamond-like sample is due to graphite present in the small domains of the microcrystalline sample.

The conclusion that the Raman bands of diamond-like films at 1355 and 1590 cm^{-1} are due to graphite bonding does not exclude the presence of regions of diamond structure. Electron energy loss experiments have shown features which can be attributed to diamond structures. The origin of the inconsistency between the two spectroscopies may possibly lie in the Raman cross section which may limit the detection of diamond forms.

The bond types of diamond thin films are substantially different from those of diamond-like films; these intrinsic differences are manifested in the Raman spectra. A Raman spectrum of microcrystalline diamond film is presented in Fig. 3.3. The spectrum shows a sharp Raman band at 1332 cm^{-1} and a broader Raman band at ~ 1500 cm^{-1}. The spectral properties of the 1332 cm^{-1} band indicate that this band is due to micron-scale domains of diamond or large regions of diamond present in the microcrystal. The 1500 cm^{-1} band, which is often referred to as the graphitic band, is ascribed to the amorphous network of sp^2 bonding (possibly combined with a smaller component of sp^3 bonding). The sp^2 amorphous network (the

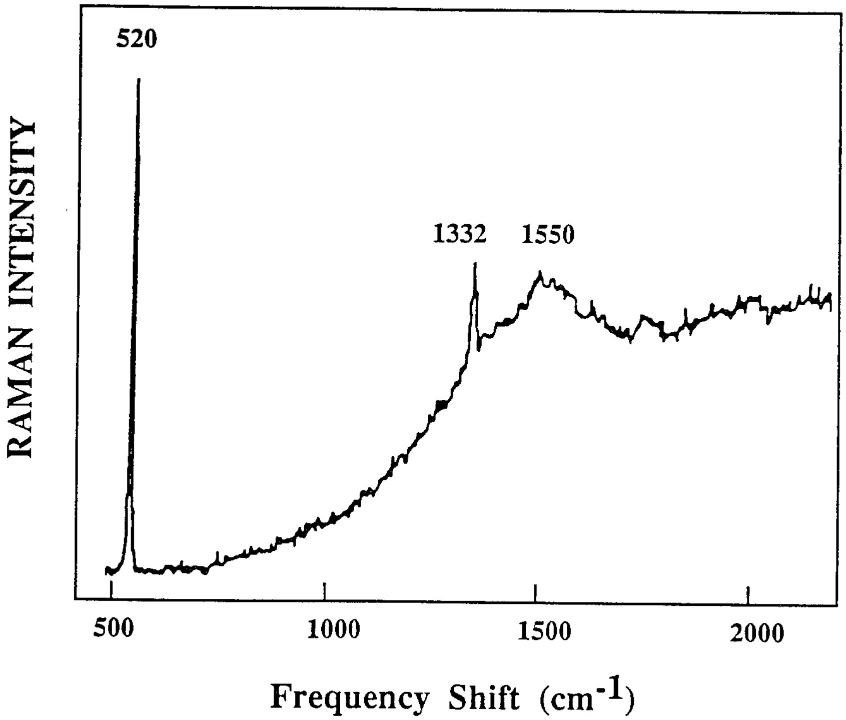

Figure 3.3 The Raman spectra of diamond film. The band at 1332 cm^{-1} is due to the diamond bonding and the band at ~1550 cm^{-1} is due to graphitic bonding. The sharp feature at 520 cm^{-1} is due to the silicon substrate [8].

graphitic phase) may exist between the diamond crystalline domains on grain boundaries or may exist as inclusions.

3.2. Analytical Raman Spectroscopy of Diamond Films

The Raman intensity may be a quantitative measure of the relative concentrations of a composite's constituents since the intensity depends on the absorption coefficient, a quantity which is dimension-related. Shroder *et al.* [9] have developed a model in which the concentrations of diamond and graphitic components (a transparent material and an absorbing material respectively) in diamond films may be obtained from the Raman intensities. The following section outlines the principal results.

The Raman intensity, I, from a material (in a backscattering geometry) has been shown by Loudon [26] to follow the relation:

$$I = \frac{I_0 S}{S + \alpha_1 + \alpha_2} \left\{ 1 - \exp\left[-\left(S + \alpha_1 + \alpha_2 \right) L \right] \right\} \tag{3.1}$$

where S is the scattering efficiency, I_0 is the incident intensity, L is the sample thickness in the direction of the incident laser light, and α_1 and α_2 are the absorption coefficients at the frequencies of the incident and scattered light respectively. Wada *et al.* [48] showed that the equation could be modified to give the ratio of the Raman intensities of two different materials:

$$\frac{I_D}{I} = \frac{I_{0D}}{I_0} \left[\frac{A_D}{A} \right] \left[\frac{L_D(\alpha_1 + \alpha_2)}{1} \right] \left[\frac{\Delta\Omega_D}{\Delta\Omega} \right] \left[\frac{1 - R_D}{1 - R} \right]^2 \left[\frac{\left\{ \sum_j \left(\hat{\mathbf{e}}_2 \bullet \mathbf{R}_j \bullet \hat{\mathbf{e}}_1 \right)^2 \right\}_D}{\left\{ \sum_j \left(\hat{\mathbf{e}}_2 \bullet \mathbf{R}_j \bullet \hat{\mathbf{e}}_1 \right)^2 \right\}} \right] \tag{3.2}$$

where S has been redefined in terms of a scattering efficiency (A), and a summation over the inner product of the Raman tensor (R_j) and the polarization unit vectors of the incident and scattered light, $\hat{\mathbf{e}}_1$ and $\hat{\mathbf{e}}_2$. I is the scattering intensity of the material being compared; I_D represents the scattered intensity from the diamond, and I_0 is the incident intensity. $\Delta\Omega$ is the solid angle into which light is scattered, and the term involving R is a correction term for reflection of the scattered light at the sample surface and multiple reflections within the sample. Here, α_1 and α_2 are the previously defined absorption coefficients of the material to be compared to diamond since it has been assumed that diamond is transparent to the visible laser radiation.

In order to investigate the Raman intensity from a composite, Shroder *et al.* [9] prepared samples consisting of compressed powder of ~1 μm diamond and ~ 40 μm graphite particles for which the concentrations in each sample were known. In order to apply Eq. 3.2 to the diamond-graphite composite samples several approximations relevant to the experimental conditions had to be made. The first approximation was that the values of L_D and $\Delta\Omega$ were the same for both materials since the Raman signal was being collected from a region of discrete particles. Moreover, the reflection losses due to light scattering between the graphite and diamond particles were assumed to be minimal and thus were disregarded. Finally, due to the random orientations of the particles, an angle-average value of the summation over all possible polarization directions was taken.

In light of these approximations, the ratio of the Raman scattering intensities of diamond to graphite may be given as:

$$\frac{I_D}{I_G} = \frac{4A'_D N_D V_D}{3A'_G N_G V'_G} = \frac{4A'_D N_D V_D}{3A'_G N_G V_G}\left[\frac{V_G}{V'_G}\right] \qquad (3.3)$$

where A' is the angle- and polarization- averaged scattering efficiency per nearest-neighbor bond, N is the atomic density and V_D and V'_G are the volumes of the diamond and graphite respectively which are sampled by the Raman scattering. The absorption factor of graphite is accounted for in the factor V'_G/V_G which represents the fraction of each graphite particle sampled in the Raman process. Such a discriminating proportionment of volume is not applicable to diamond since it is essentially transparent to the laser light, so the entire volume of diamond is sampled by the Raman scattering. The factor of 4/3 accounts for diamond having four nearest neighbors and graphite having three nearest neighbors at each site. Equation 3.3 can be written in terms of the percentage of diamond in the composites, P_D, as follows:

$$\frac{I_D}{I_G} \sim \frac{4A'_D}{3A'_G}\left[\frac{P_D}{1-P_D}\right]\left[\frac{V_G}{V'_G}\right]. \qquad (3.4)$$

At 514.5 nm laser excitation, graphite has an absorption depth of ~30 nm [48]. However, because the scattered light must also exit the absorption region, an absorption length of ~15 nm was considered instead (see Fig. 3.4A). The ratio of the scattering efficiencies, A'_D/A'_G, was taken to be ~1/75.

Equation 3.4 states that for a given composite the relative Raman intensities are modulated not only by the relative Raman scattering efficiency but also by the volume of the absorbing component, which is actually sampled by Raman scattering. The effect of the absorption on the Raman spectra can be seen qualitatively in the spectra presented in Fig. 3.4B. In the figure, the spectra of diamond-graphite composites (of ~1 μm diamond and ~40 μm graphite particles) are shown for which the relative concentration of diamond in the samples ranges from ~1% up to 60%. An interesting aspect of these spectra is that the ~1% diamond composite displays a 1:1 ratio between the peak intensities of diamond and graphite. At 50% diamond concentration, it can be seen that the peak due to graphite has practically disappeared even though the Raman cross section is 75 times larger in graphite than in diamond. Thus the absorption of graphite has a significant effect on the Raman spectra of the composites, as is shown in the large disparity of the measured intensities of the samples.

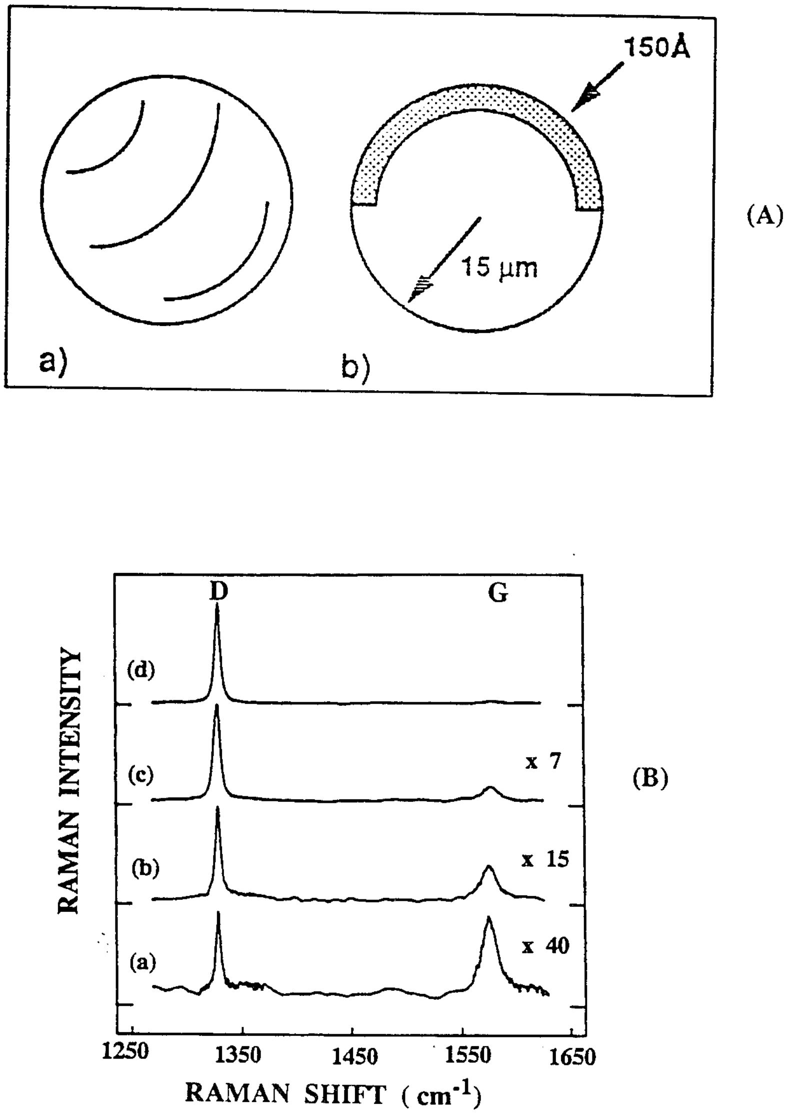

Figure 3.4 (A) Model of the unit volumes in the Raman scattering from composites. (a) fully illuminated diamond particle of ~ 30 µm size and (b) graphite particle ~ 30 µm size, partially illuminated in a 15 nm surface layer. (B) The Raman spectra of the composites of diamond and graphite powders. The relative concentrations of diamond in the samples are (a) 1.3%, (b) 6.6%. (c) 21.5%, and (d) 50%. The diamond band (D) is at 1332 cm^{-1} and the graphite band (G) is at 1580 cm^{-1}. From Shroder *et al.* [9].

The quantitative predictions of the model, as given in Eq. 3.4, are evidenced in Fig. 3.5, where the ratio of the two peaks versus concentration of diamond is plotted for various particle sizes of graphite. It can be seen in the figure that when the particle size was taken to be 42 µm, the model and the experimental data are in agreement. Within the model, when the graphite domains are smaller than the absorption length, the value of V'_G/V_G becomes 1 and the effect of absorption can be ignored. The only intensity-modulation factor in that case is the relative Raman scattering efficiency. In high-quality diamond film, the graphitic domains are very small, so in applying the model in most cases the absorption effect may similarly be ignored.

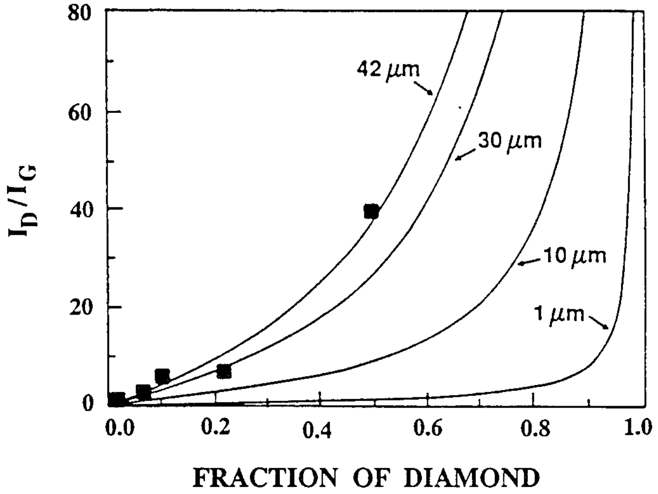

Figure 3.5 Ratio of peak intensities (I_D/I_G) vs relative concentration of diamond in the composite samples. The solid lines are derived from Eq. 3.4 assuming an average graphite particle size of 42, 30, 10, and 1 μm, respectively [9].

3.3. The Diamond Raman Lineshape of Diamond Films

The Raman frequency of a high quality material yields information about the vibrational energy of the phonons whereas the Raman linewidth is a measure of the phonon-lifetime. When the quality of a material is degraded due to the presence of defects, the resulting Raman lineshape reflects the effect of the defects on the phonon-characteristics. The focus of this section is recent investigations of Raman lineshape as it relates to the various defects which are present in diamond thin films.

The Raman linewidth in general can be broadened via several mechanisms: the main mechanisms applicable to the diamond line are homogeneous broadening [28] and broadening due to the size effect of the crystal, a theory which has been developed to explain the lineshape of boron-nitride material [29]. Homogeneous broadening arises from a decrease of the lifetime of the crystal phonons. The theory of homogeneous spectral lineshape predicts that the linewidth is inversely proportional to the phonon lifetime and that the lineshape is expected to be a Lorentzian [27]. The other possible mechanism which results in Raman line broadening is phonon confinement in a small domain size [29].

The well-established confinement model is based on the uncertainty principle, $\Delta k \sim 2\pi/d$, which states that the smaller the domain size d, the larger the range of different phonons (with different q vector and different energy) that are allowed to participate in the Raman process. Hence the broadening of the Raman line in this case is due to the spread in phonon energy, and the lineshape reflects the shape of the phonon-dispersion curve. The Raman lineshape in the phonon-confinement model is given by

$$I(w) \cong \int_0^1 \frac{dq \exp(-q^2L^2/4)4\pi q^2}{[\omega-\omega(q)]^2+(W_0/2)^2} \tag{3.5}$$

where L is the confinement size, W_0 is the diamond natural linewidth (~2 cm^{-1}), and $\omega(q)$ is the phonon-dispersion curve of the form $A+B\cos(q\pi)$ [29, 52-54]. In general the width, shape, and peak position are dependent on phonon dispersion curves. In particular for silicon, the above model predicts that as the Raman line gets broader, the peak of the line shifts to a lower frequency and the lineshape becomes asymmetric [53].

Ager *et al.* [52] have investigated the application of the confinement model to the Raman lineshape of diamond thin films. For each of the relevant phonon-dispersion relations, Ager *et al.* modeled the expected lineshape using the confinement model (Eq. 3.5) and compared the results to the Raman lineshape of diamond films. The study of the expected Raman line involved three sets of lineshape calculations in which different one-dimensional dispersion curves were used. First, in case (a), a dispersion relation was used for which the phonon frequency decreases away from the Γ point. The dispersion relation has the form $\omega(q)=A+B\cos(q\pi)$, where A=1241.25 cm^{-1} and B=91.25 cm^{-1}; the shape of this curve is similar to that used in Si and GaAs phonon-confinement calculations. For case (b) the Δ_2 (O) dispersion curve was used; this curve in diamond has a shallow maximum which is farther from the Γ point. Figure 3.6 depicts the characteristics of the first two dispersion relations [55]. Lastly, in case (c) the weighted averaged 3D dispersion curve was used in the calculations (see [52] for a more detailed analysis).

Figure 3.7 presents the Raman linewidth vs. the Raman frequency, as obtained from Eq. 3.5, for the three cases of dispersion relations. The Raman linewidth vs. frequency-correlation which was obtained from diamond films is also presented in the figure. Figure 3.8 shows the predicted Raman lineshapes as calculated from the phonon confinement theory for various values of domain size, L, and for dispersion relations (a) and (b). In Fig. 3.9 the Raman spectra of diamond films and crystal are presented. As can be seen in the figures there is no agreement between the Raman diamond lineshapes obtained from diamond films (which are symmetric) and those predicted from the confinement model (which are asymmetric). From these results Ager *et al.* have concluded that the size effect in diamond films is not a dominant factor in determining the lineshape characteristics of diamond films. They suggested that the

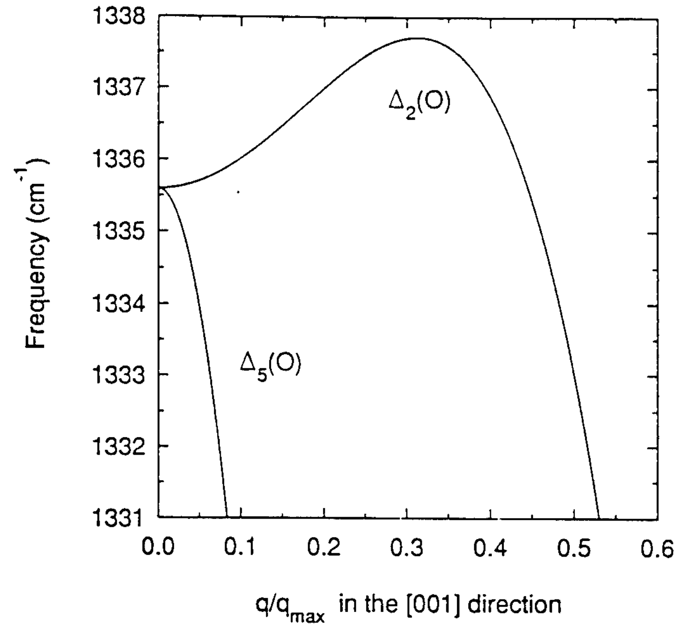

Figure 3.6 Detail of the (001) phonon-dispersion curves for diamond [52]. The Δ_5(O) has a maximum at Γ point. The Δ_2(O) curve exhibits a shallow maximum away from the Γ point. From Ager *et al.* [52].

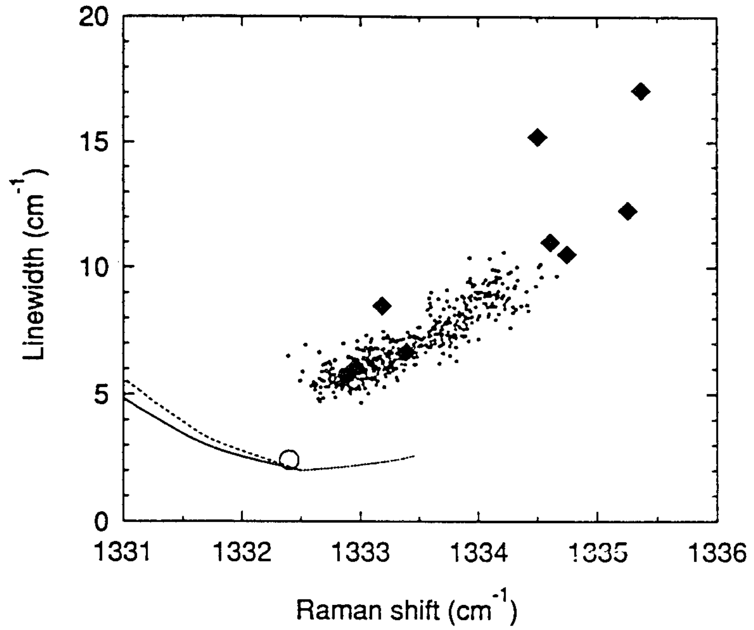

Figure 3.7 Raman linewidth vs Raman frequency for diamond: (circle) single-crystal; (diamonds) single-point measurements from ten diamond films; (dots) 500 spatially resolved measurements from one sample; (solid lines) phonon-confinement theory as predicted from case (a); (dotted line) the predicted model case (b), and (long dashes) of case (c). The experimental linewidth is an increasing function of the Raman peak position, an opposite behavior to the one expected from the confinement model. From Ager *et al.* [52].

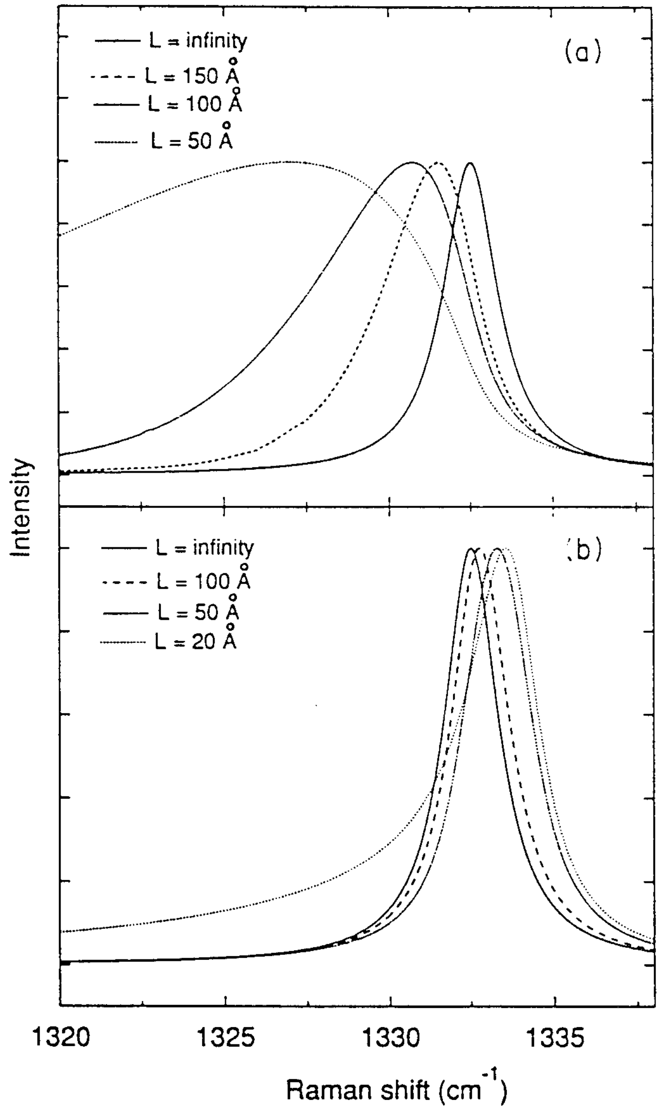

Figure 3.8 Calculated Raman lineshapes from the phonon confinement theory for different values of domain size L. (a) results when using dispersion relation described in case (a), (b) the results of case (b). From Ager *et al.* [52].

internal compressive stress in diamond is a more likely mechanism in determining the Raman line shape. Results similar to those obtained by Ager *et al.* also have been reported by Bergman *et al.* [15]; moreover, in the latter study the Raman lineshape was found to be correlated to the internal compressive stress imposed, for most part, by the graphitic phase present in the diamond thin films.

3.4. The Effect of the Graphitic Phase on the Luminescence of Diamond Films

This section presents a study of the broadband and the nitrogen-related luminescence in CVD diamond films [56]. A broadband luminescence extending from approximately 1.5 to 2.5 eV and centered at ~ 2 eV has been observed in various PL studies of diamond films [57, 58]. A complete model has yet to be formulated to explain the origin of this broadband PL. Studies

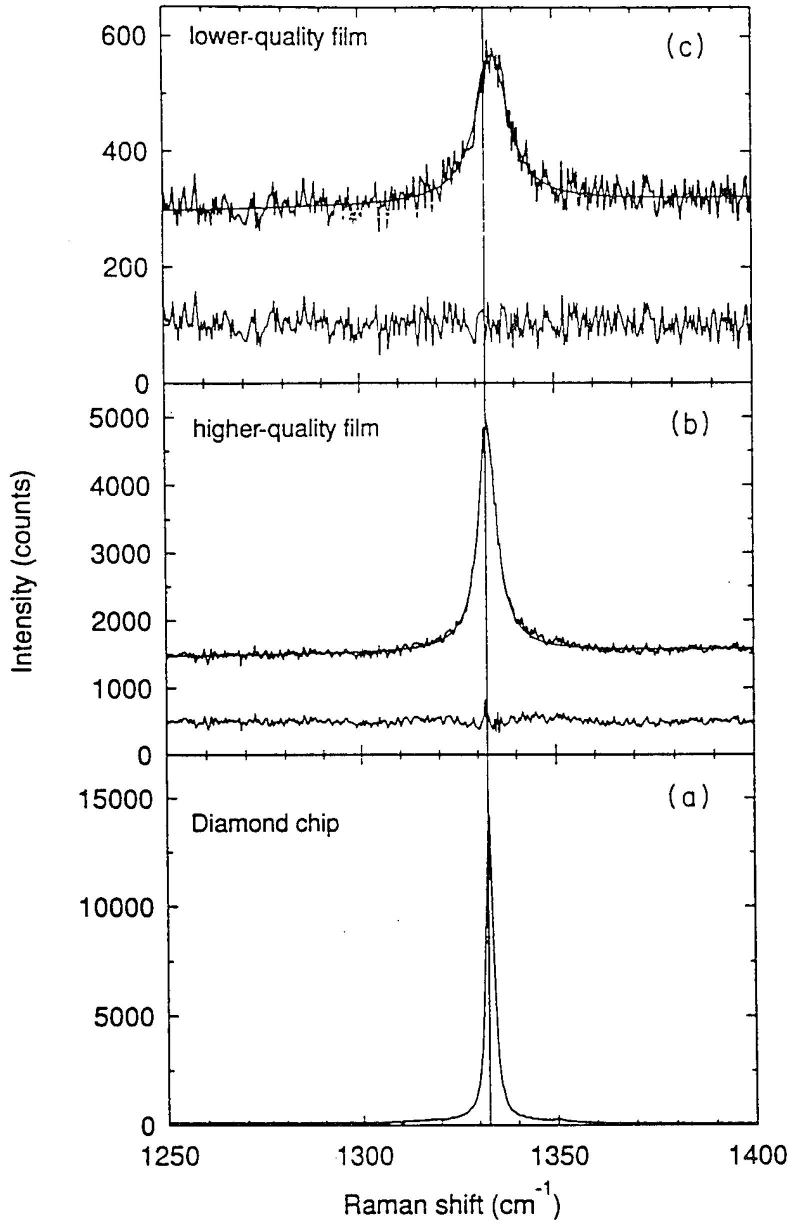

Figure 3.9 Raman spectra of diamonds. (a) Type IIa synthetic diamond. (b) High quality diamond film, and (c) lower-quality diamond film. The lines exhibit a Lorentzian lineshape. From Ager *et al.* [52].

utilizing cathodoluminescence (CL) and absorption spectroscopy of crystal diamonds of types Ia and Ib which contain nitrogen have shown that similar luminescence has its origin in the electron-lattice coupling (vibronic interaction) of nitrogen related centers with zero phonon lines (ZPL) at 1.945 and 2.154 eV [59, 60]. Luminescence studies on natural brown diamonds [61] have shown that the brown diamonds luminesce in the yellow and in the red region of the spectrum. The luminescence appears in the optical spectra as wide bands centered at ~ 2.2 eV and at ~ 1.8 eV and is very similar to the one observed in the spectra of the CVD diamond films. The origin of the PL bands of the brown diamonds has also been determined to be of vibronic nature with numerous ZPL the principal ones at 2.721 and at 2.145 eV [61, 62].

An alternative mechanism which could give rise to the broadband PL in the CVD diamond films is the amorphic phase of the sp^2-bonded carbon (also called the graphitic phase), the presence of which has been widely confirmed. The PL of amorphous carbon films exhibits an emission centered at ~ 1.8-2 eV which is of similar line shape to that observed in the diamond films [49, 63]. According to the general model of the state distribution of amorphous materials [64] the distortions of bond angles and of bond lengths which constitute the amorphous phase introduce a continuous state distribution in the optical band gap of the material. The PL of amorphous carbon films has been suggested to originate in the optical transitions of an in-gap state-distribution related to the disordered forms of the sp^2 carbon bonding [49].

In a study which is outlined here, the presence of an in-gap state-distribution due to the sp^2 bonding has been established, and was suggested to be the likely cause of the broadband luminescence [56]. The first part of the study focused on obtaining the PL spectra of nitrogen-doped and undoped diamond films, identifying the nitrogen-related PL bands, and examining the influence of the nitrogen on the broadband PL. In Figure 3.10, the PL spectra of the nitrogen doped and undoped diamond films are shown. Both spectra were obtained utilizing the 514.5 nm green line of the Argon laser. The PL spectra are shown on an absolute energy scale. The PL spectrum of the undoped diamond film exhibits the fairly smooth broadband line shape centered at ~ 2.05 eV, and also exhibits the 1.681 eV band which has been attributed to an optical transition in a Si complex center [65]. However, the spectrum of the nitrogen-doped film indicates a red-shift of the broadband luminescence as well as a line-shape change. Furthermore, the nitrogen-related bands at 2.154 and 1.945 eV are present. Studies carried out by Davies *et al.* [60] have suggested that the 1.945 eV band is due to the substitutional nitrogen-vacancy optical center. Collins *et al.* [59] proposed that the 2.154 eV band is the result of a transition in a center consisting of a single substitutional nitrogen atom with one or more vacancies. Yet another PL band at 1.967 eV is also present in the spectrum (barely distinguishable from the 1.945eV band), which might also be due to a nitrogen-related center.

In order to examine in further detail the line-shape of the broadband PL, the 457.9 nm blue laser line was used for excitation. Figure 3.11 shows the spectra of the nitrogen doped and undoped diamond films for this laser frequency. The broadband PL of the undoped diamond film retained its relatively unstructured line-shape; however, the maximum intensity is shifted towards higher energy and is centered at ~ 2.2 eV. The spectrum of the nitrogen-doped diamond film exhibits the nitrogen-related bands at 2.154 and at 1.967 eV. The 1.945 eV band, which appeared with the 1.967 eV band as a doublet in the spectrum obtained using the green

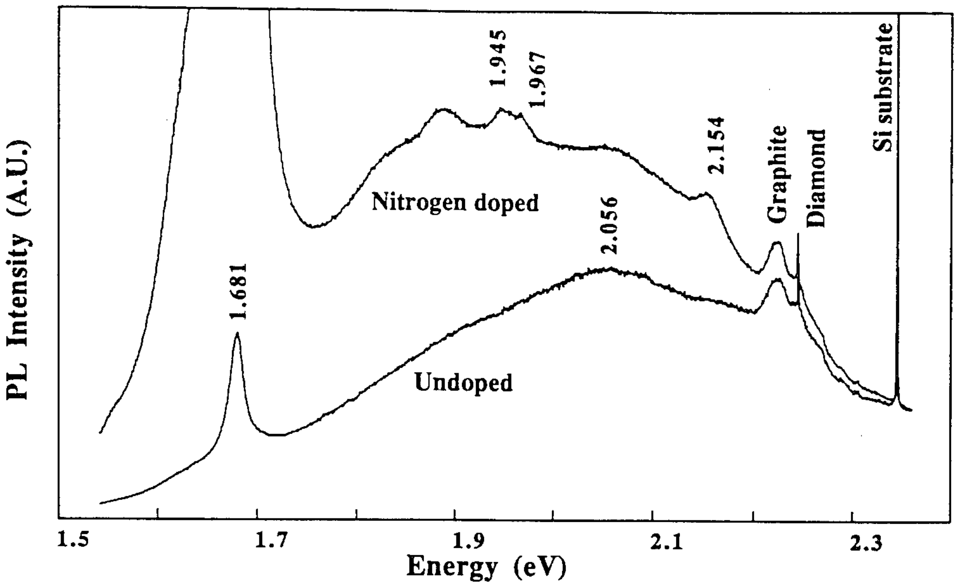

Figure 3.10 The PL spectra of the nitrogen doped and of the undoped diamond films employing the 514.5 nm laser line. Raman bands are labeled as to origin and the peak energies of the PL bands are indicated. The PL nitrogen-related-centers at 1.945, 1.967, and 2.154 eV are present in the spectrum of the nitrogen doped sample. From Bergman *et al.* [56].

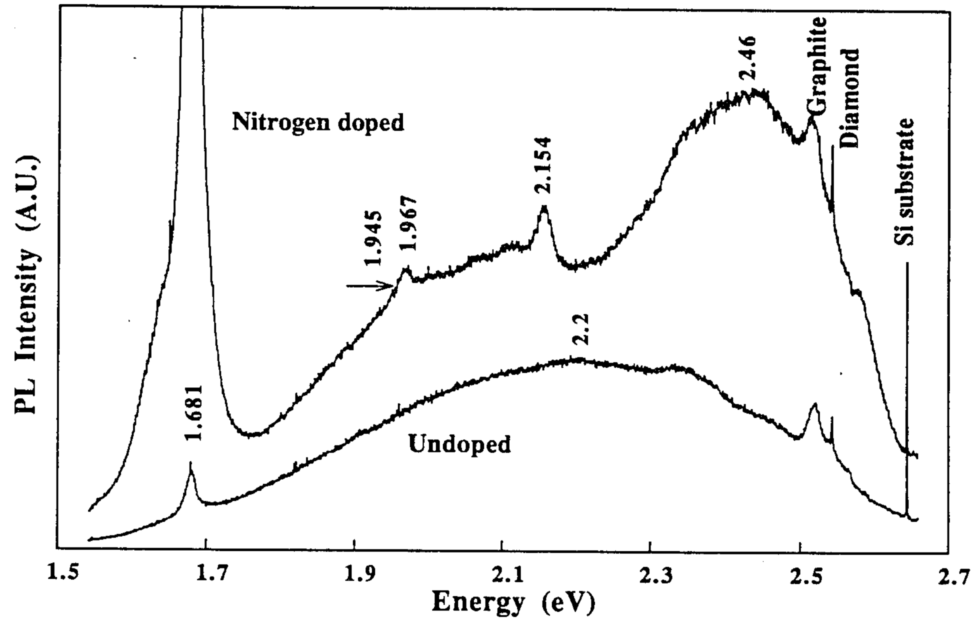

Figure 3.11 The PL spectra of the nitrogen doped and of the undoped diamond films employing the 457.9 nm blue laser line. The PL nitrogen-related-centers at 1.945, 1.967, 2.154, and at 2.46 are present in the spectrum of the nitrogen doped sample. The spectrum of the undoped sample consists of broadband luminescence. From Bergman *et al.* [56].

laser line, cannot be clearly distinguished in the spectrum taken using the blue line. The overlapping of the two bands is a resolution artifact of the scaling of the spectrum taken using the blue laser line. A relatively wide band with line-width ~ 0.3 eV centered at 2.46 eV is also present. Similar wide-band cathodoluminescence has been observed in both natural and synthetic diamonds, and is commonly referred to as "green band A" luminescence [66]. It is evident from the spectra in Figs. 3.10 and 3.11 that the incorporation of nitrogen caused a distortion in the line-shape of the underlying broadband luminescence. If the broadband PL had been due to a nitrogen-lattice interaction, the line-shape would have been invariant, and a change in the intensity would have been anticipated.

3.4.1 The Temperature Characteristic of the Broadband PL

A second series of experiments and analysis were also conducted to further rule out the possibility of the broadband PL being of vibronic origin [56]. According to the theoretical model of the electron-lattice interaction [32, 67], the total band intensity which includes the zero-phonon line and its vibronic sideband is expected to be independent of temperature. As the temperature increases the zero-phonon line intensity decreases, and the vibronic band intensity is expected to increase so as to keep the total intensity constant with temperature (where the ZPL and sideband intensities are taken relative to the total band intensity). The width of the vibronic band is also expected to increase with temperature. However, as shown in Fig. 3.12 it was found instead that the broadband PL intensity of the undoped sample exhibits a ~ 60% decrease with increasing temperature without any significant change in the band width. Furthermore no ZPL lines were present at the low temperature spectra. However, the ZPL responsible for the vibronic band in brown diamonds as well as the ZPL of nitrogen centers are known to be sharp and well-pronounced in low-temperature spectra [66]. The temperature dependence observed is thus not characteristic of a vibronic interaction.

Figure 3.13 shows the correlation between the Raman intensity of the graphitic phase and the intensity of the broadband PL. This correlation was found and described in detail in a previous study [57]. It was found that, as a function of growth time, as the graphitic phase increases so does the intensity of the broadband PL. It has been suggested that the amorphic graphitic phase introduces a state distribution in the band gap which provides transition centers for the photo-excited carriers, thus resulting in the broadband PL.

In order to prove the above postulate, a further investigation of the broadband PL had to be carried out. In general the PL process can be expressed by the following equation

$$I / I_0 = P_R / (P_R + P_{NR}) \qquad (3.6)$$

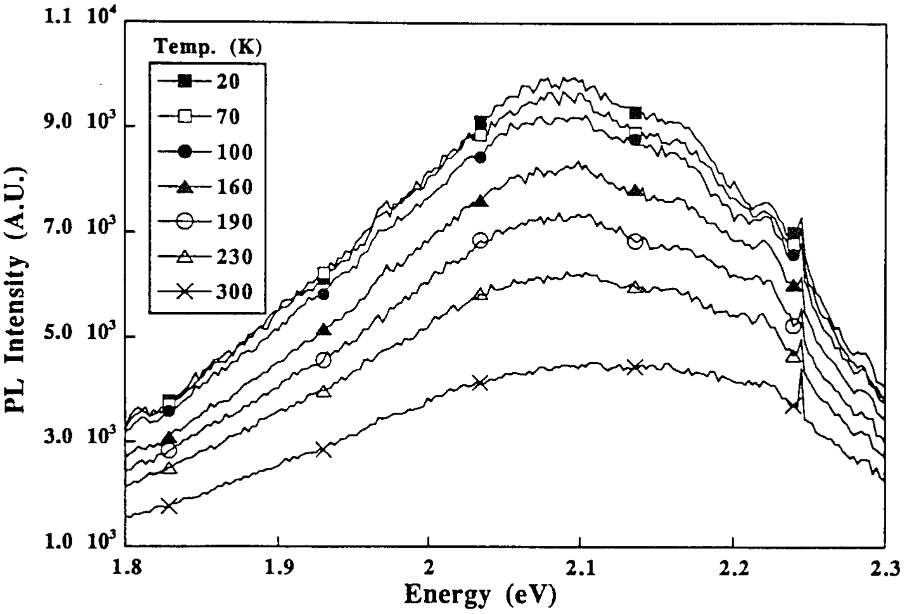

Figure 3.12 The spectra of the broadband PL of the undoped diamond sample at various temperatures. The spectra do not exhibit any phonon lines. From Bergman *et al.* [56].

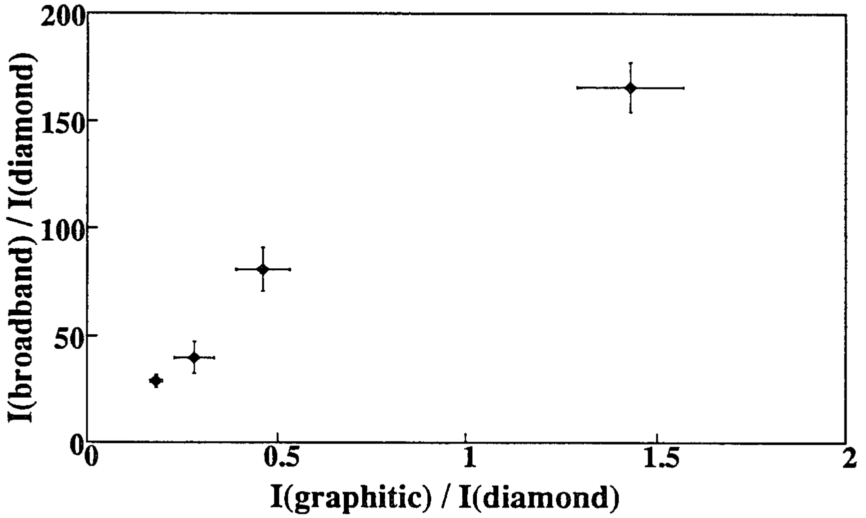

Figure 3.13 Correlation between the broadband PL intensity and the graphitic Raman intensity. Intensities of PL were normalized to the diamond Raman intensities. From Bergman *et al.* [56].

where P_R and P_{NR} are the probabilities for the radiative and the nonradiative recombination respectively [31], I is the PL intensity, and I_0 is the PL intensity for the temperature approaching absolute zero. If there exists a single activation energy E_A for P_{NR} for which the thermal quenching of the PL is of the form of a Boltzmann activated process then Equation (3.6) becomes:

$$P_{NR} / P_R = [I_0 / I(T)] - 1 \sim \exp(- E_A / k_B T) \tag{3.7}$$

By plotting $\log((I_0 / I(T) - 1))$ vs. $1/T$ a straight line should be obtained from which E_A can be evaluated. Figure 3.14 shows this plot for the experimental data, I(T), the inset in the figure shows I(T) vs. temperature. The continuous curve of Fig. 3.14 indicates the existence of a continuous distribution of activation energies E(T) rather than a single E_A associated with one energy level of a specific defect. Such a continuous distribution of activation energies E(T) indicates in turn a corresponding distribution of localized energy states in the band gap of the diamond film. E(T) may thus be viewed as corresponding to the binding energies of these localized states. The data in Figure 3.14 can be fitted by the equation

$$[I_0 / I(T)] - 1 \sim \exp(T/T_0) \tag{3.8}$$

for which T_0 is a constant to be determined. This form of quenching of the PL has also been observed and its theory developed by Street *et al.* [68] in their extensive work on amorphous Si:H. It should be noted that the broadband PL intensity in the diamond films exhibits a much slower decrease with increasing temperature than the PL intensity reported for a-Si:H. A smaller dependence on temperature was also reported for amorphous C:H [63] with temperature dependence of the form of Equation 3.8, consistent with the findings presented here. According to the model developed by Street *et al.* for amorphous materials T_0 is a measure of the width of an exponential in-gap state distribution from which optical transitions can occur [68]. More extensive experiments need to be carried out to further quantify and model the state distribution and to determine the bands involved in the optical transitions. In amorphous carbon material the sp^2 bonding creates sigma-bands (σ, σ^*) and pi-bands (π, π^*)

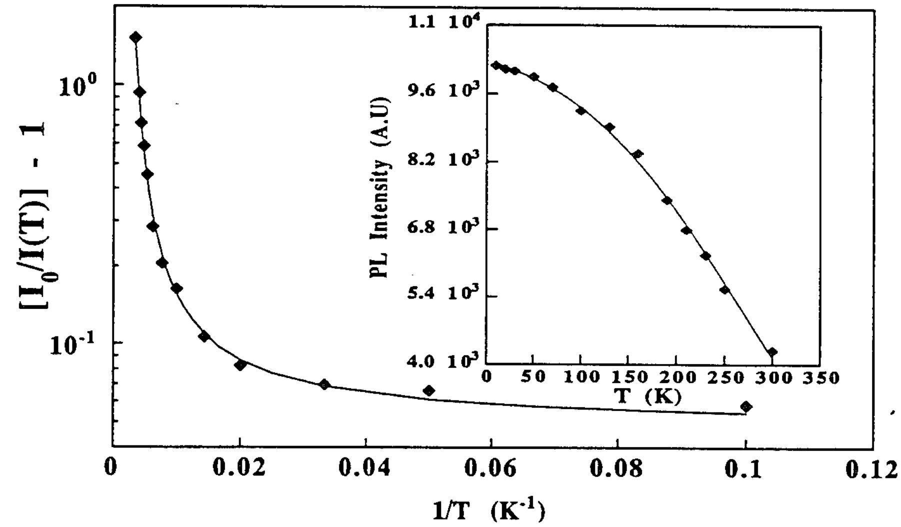

Figure 3.14 The functional behavior of the broadband PL vs 1/T as obtained from the undoped diamond sample. From Bergman *et al.* [56].

for which optical transitions can occur [49]. At present it is hypothesized that the π-π* band transitions are responsible for the broadband PL; these bands constitute allowable optical transitions and are in the energy range closest to the laser excitation energy.

In summary, the spectra of both nitrogen-doped and undoped films exhibited the broadband PL; the nitrogen-doped sample, however, had a distortion of the line-shape of the underlying broadband PL due to the vibronic interaction of the nitrogen centers. The nitrogen optical centers at 2.154, 1.945 and at 2.46 eV (the green band-A) were observed, as well as a new possibly nitrogen-related center at 1.967 eV. The temperature behavior of the broadband PL indicates that the band does not originate from a vibronic interaction. Moreover, the intensity of the broadband PL was found to exhibit a temperature dependence characteristic of optical emission from a continuous distribution of gap states. In light of the above findings and from the correlation of the PL intensity to the graphitic phase it is suggest that the broadband PL in diamond films is due to the optical transitions in an in-gap state distribution, where the in-gap state distribution is introduced by the amorphous phase of the sp^2 hybrid bonding.

Complementary studies of the origin of the broadband PL were recently carried out by Dallas *et al.* [69] and by Gangopadhyay *et al.* [70] utilizing time-resolved photoluminescence (TRPL) spectroscopy. In these studies the researchers measured the PL decay times for undoped and nitrogen-doped diamond films as well as the decay time of an hydrogenated amorphous carbon (a-C:H) film. The decay times of the undoped diamond film were measured at several energies in the 1.55-2.07 eV range of the broadband PL. The analysis indicated that the decay times at the various energies of the broadband PL are of the same magnitude, ~1.62 ns. A similar decay time (1.69 ns) was measured for the PL band of the a-C:H film. The nitrogen-doped decay time, on the other hand, was found to vary with the PL energy, and was dominated by the decay time of the nitrogen centers at the specific energy; at emission energies 2.15, 2.07, 1.95 and 1.55 eV the measured lifetimes are 25.6, 24.9, 14.9 and 11.4 ns respectively. The decay times of the nitrogen-doped film were much longer than those of the undoped diamond film.

The comparable decay times of the undoped diamond film and the a-C:H film led the researchers to conclude that both materials exhibit similar radiative recombination centers [69]. Hence the broadband PL in the undoped diamond film was concluded to be of similar origin as the PL of the a-C:H film.

4. The Nitrogen Optical Centers

4.1. The Forms of Nitrogen Impurities and Optical Centers in Diamond

The two main forms that nitrogen impurities assume in the diamond lattice are the single substitutional nitrogen and the nitrogen-A aggregates [66, 71]. Natural and synthetic diamonds containing the A aggregate are referred to as type Ia diamonds while those containing the single substitutional are type Ib diamonds. The energy level of the single substitutional nitrogen lies ~ 1.7 eV from the conduction band; the center is not luminescence active and its presence in the diamond can be detected via absorption and electron paramagnetic resonance spectroscopy [66]. Moreover, due to the large ionization energy of the single substitutional nitrogen the center is not an active donor.

The A aggregate, which consists of two nearest-neighbor nitrogen atoms and has trigonal symmetry, is a very common form of nitrogen in natural diamond [72-74]. The trigonal symmetry of the A aggregate is depicted in Fig. 4.1, where X and Y represent the nitrogen atoms. The energy level of the A aggregate lies ~4 eV from the conduction band and like the single substitutional impurity center, the A aggregate is not a luminescence active center but can be detected via absorption spectroscopy.

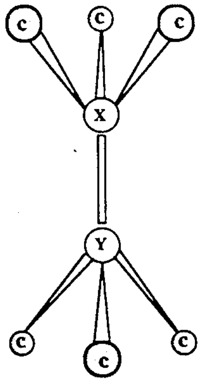

Figure 4.1 The trigonal symmetry. The "c" represent the carbon atoms. For the A aggregate the X and Y represent the nitrogen atoms, while for the 1.945 eV optical center the X and Y represent the nitrogen atom and vacancy respectively.

In general, when nitrogen atom(s) from the single substitutional or from the A aggregate are combined with vacancies, luminescence centers are created in the diamond. There are many nitrogen related optical centers in diamond with emission energies spanning the visible spectrum [66, 71, 75]. A short summary of optical centers relevant to this review is given below.

The 1.945 eV PL band arises from transitions in optical centers which consist of a substitutional nitrogen atom and a vacancy at a nearest neighbor site; the center's symmetry has been suggested to be trigonal C_{3v} [66, 76]. Figure 4.1 presents the structure of the 1.945 eV optical center; the C's represent the carbon atoms and the X and Y represent the nitrogen atom and vacancy respectively. The 1.945 eV center has been observed in crystal diamond as well as in nitrogen doped diamond films. The actual energy level of the 1.945 eV center in the diamond bandgap is as yet unknown. However, it has been established that the transitions of this optical center are between excited and ground states of a deep state that lies in the diamond gap [66].

The other optical center which is common to both diamond crystals and nitrogen doped films is the 2.154 eV. The symmetry of this center has been suggested to belong to one of the trigonal subgroups and the structure to consist of a single nitrogen atom and one or more vacancies [59, 77]. Like the 1.945 eV center, the 2.154 eV is considered to be a deep level optical center of intra-impurity transitions.

The 2.462 eV (H3) optical center is one of the most commonly observed centers in natural and synthetic diamond [66]. The structure of the H3 optical center consists of two nitrogen atoms from the A aggregate and one vacancy. Recently Collins *et al.* have detected the H3 cathodoluminescence line from a single particle of CVD diamond, implying that small concentrations of A nitrogen can be present in this material [71].

The band A luminescence has been observed to be present in the spectra of crystalline diamonds as well as in that of nitrogen-containing diamond films. The band A luminescence is relatively wide (~0.5 eV) and its peak position has been reported to vary from ~2.3 - 2.7 eV depending on the diamond type [1, 75, 78-81]. It has been proposed that the band A PL could be a result of donor-acceptor pair recombination transitions [82]. In the proposed mechanism the donor has been suggested to be one nitrogen atom of an A aggregate and the acceptor to be the boron impurity.

The energy released via the donor-acceptor transitions can be expressed as a Coulomb interaction of the form

$$E(r) = E_G - (E_D + E_A) + B/r \qquad (4.1)$$

where E_G, E_D and E_A are the diamond gap, donor and acceptor ionisation energies respectively, r is the separation of the donor and the acceptor in the diamond matrix, and B is a constant. Hence the resulting luminescence lineshape reflects the distribution of the donor-acceptor separation in the crystal. The energy level E_D of the A aggregate is positioned ~1.5 eV from the valence band and the energy level of the boron E_A is ~0.37 eV from the valence band [66]. Figure 4.2 schematically presents the energy levels of the donor and the acceptor in the diamond gap. It should be noted that the donor-acceptor model is widely regarded as the most likely mechanism responsible for the band A luminescence, although further experimental evidence is required to establish its certainty. The only strong correlation that has been established is between the existence of the nitrogen-A aggregates in the diamond and the presence of the band A in the PL spectra [66].

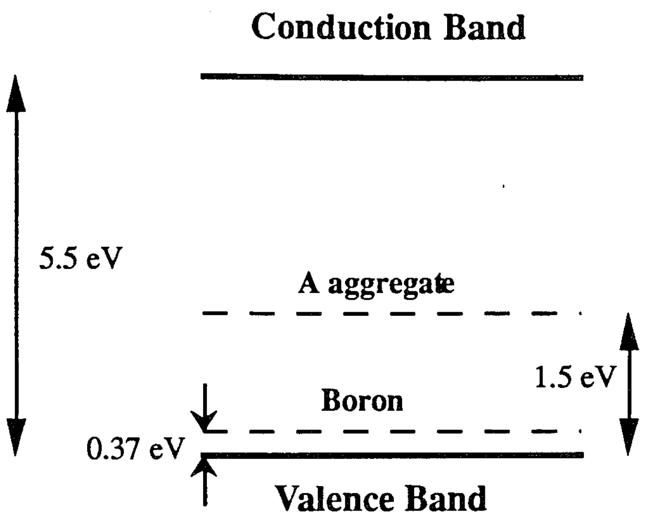

Figure 4.2 The energy levels of the A aggregate and Boron donors in the band-gap of the diamond.

4.2. Correlation of the Band-A Luminescence to Structural Defects

Two luminescence broad bands have often been observed in the spectra of crystalline diamonds as well as in diamond films: a blue band with peak in the range 2.6-3 eV and a green band with peak in the range 2.2-2.5 eV, referred to as the blue band-A and the green band-A respectively. Both bands have been suggested to originate from the donor-acceptor radiative recombination mechanism. The occurrence of the blue and the green bands, according to the model, depends on the mean separation of the donor-acceptor pairs: the blue emission corresponds to the closely spaced pairs while the green emission is due to transitions between the more widely spaced pairs. It has been argued that in natural diamond the donor-acceptor close pairs resulted from diffusion of the impurities at elevated temperatures over periods of millions of years. As has been noted by Collins *et al.* [65, 83], it is not immediately evident how such close pairs can be produced during the growth of CVD diamond.

The blue band-A is of a great interest due to the established correlation between its emission line and the presence of dislocations in the diamond [84-86]. Yamamoto *et al.* [86] have developed a technique which allows both high-resolution transmission electron images and optical emission (CL) to be acquired from the same isolated dislocation. This type of spectroscopy is advantageous in the investigation of a nano-scale structure since it also conveys information about the optical properties of the structure. In the experiments by Yamamoto *et al.* it was observed that dislocations in natural diamonds emit the blue band-A CL at ~2.8 eV. The luminescence lineshape characteristic was found to be similar for screw and edge dislocations, and the luminescence exhibited polarization along the dislocation line. It was suggested that the blue emission from the dislocations may be due to recombination of donor-acceptor close pairs which are arranged with variable spacing along the dislocation cores.

Graham *et al.* [80, 87] found a direct correlation between the blue band-A CL ~2.9 eV and the presence of dislocations in CVD diamond films. In their work they obtained TEM images of defect-free grains and of grains with dislocations, and the corresponding CL spectra of each grain. The band-A CL was found to be prominent only in the spectra of the grains which contained the dislocations, an observation which is consistent with that reported for bulk diamond. Although the aforementioned experimental findings clearly indicate the existence of luminescent dislocations, the actual mechanism of the luminescence is as yet uncertain; the suggested donor-acceptor model in particular bears further investigation.

4.3. Optical Analysis of Stress Sources in Diamond

4.3.1. Luminescence and Crystal Stress

General Aspects. In diamond crystal at low temperatures the PL lineshape is determined almost entirely by the crystal strain inhomogeneities. The inhomogeneous broadening is at least 1000 times greater than the homogeneous broadening [72], the latter of which arises from the life time characteristics of the transition rate. In general, the principal mechanism of the inhomogeneous broadening at low temperatures is the strain broadening that arises from the presence of dislocation type defects and/or point defects in the crystal [72, 88-90]. The defects introduce strain fields throughout the crystal that interact with and perturb the energies of the optical transitions. The statistical distribution and density of the optical centers and defects in the crystal as well as defect type determine the variations in the transition energies of the optical centers and the respective PL lineshape.

The general theory of the strain-line broadening is discussed in detail by Stoneham [90]. A brief summary of Stoneham's relevant results is presented below.

(a) For a symmetric lattice, in which the lattice sites accommodate at random the optical centers and defects, the lineshape is expected to be symmetric.

(b) When the strain in the crystal arises solely from uniformly distributed point defects the luminescence lineshape, $I(\omega)$, is expected to be a Lorentzian of the form:

$$I(\omega) = I_0 / \{1+ [A(\omega-\omega_0)/W_L]^2\} \qquad (4.2)$$

were W_L is the Lorentzian linewidth, ω_0 is the center frequency, and A is a constant.

(c) When the sources of strain in the crystal are uniformly distributed dislocations (line type defects) the lineshape is expected to be a Gaussian with linewidth W_G:

$$I(\omega) \sim I_0 \exp\{ -[B(\omega-\omega_0)/W_G]^2 \} \qquad (4.3)$$

(d) In the case when both types of defects are present in the crystal, the resulting line is the convoluted lineshape of the Gaussian and the Lorentzian: this lineshape is known as the Voigt profile and has no closed-form mathematical expression. The relative linewidths of the

Gaussian component and the Lorentzian component in the Voigt profile, W_L/W_G, reflect which defect is the source of dominant stress in the crystal.

The above results of Stoneham assumed an ideal continuous single crystal for which linear elasticity applies. Experimental evidence supporting Stoneham's work has been found which correlates the lineshape of the luminescence to the defect type, to the defect concentration and to the distribution of the defects [[88, 90] and references within.]. The above optical analysis of crystal stress and strain has proven to be useful, particularly in the cases when an appreciable amount of point defects as well as dislocations are present in the crystal [[88] and references within.].

4.3.2. The A-aggregate as Source of Stress in Natural Crystalline Diamond

Davies [72] has investigated the 503 nm (2.462 eV) PL lineshape of natural diamond crystals containing different concentration of nitrogen. According to Stoneham's theory, the expected PL lineshape should be a Voigt profile for which the Lorentzian linewidth, W_L, would be different for each sample reflecting the amount of nitrogen (point defects) in a given crystal. As a result, the ratio W_L/W_G for each of the PL lines is expected to have a different value. However, Davies found that the spectral lineshape of many of the diamonds is a Bi-Lorentzian function with linewidth W_{BL}:

$$I(\omega) = I_0 / \{1+ [A(\omega-\omega_0)/W_{BL}]^2\}^2 \tag{4.4}$$

This lineshape lies midway between the Lorentzian and Gaussian shapes and is close to a Voigt profile with Lorentzian and Gaussian components whose ratio $W_L/W_G \sim 0.5$ is independent of the nitrogen concentration. Moreover, the Bi-Lorentzian linewidth W_{BL} was found to be directly correlated with the nitrogen concentration.

The results of Davies imply that the stress contribution of line defects is negligible and that the broadening mechanism is controlled entirely by the presence of nitrogen. In order to explain the effect of the stress due to nitrogen impurities on the optical centers, as manifested in the observed Bi-Lorentzian lineshape, Davies suggested a new model which modifies Stoneham's original theory. The model basically consists of imposing a restriction on the continuum elasticity assumed in Stonehams' theory, as well as postulating on the basis of strong experimental evidence that the nitrogen is in the form of the A aggregate. The former restriction consists of requiring a critical distance between the optical center and the nitrogen defect which exerts the strain. The main conclusions of Davies are that in the case when the strain field in crystalline diamond is predominantly due to the aggregates of nitrogen, the discrete nature of the crystal has to be taken into account. The resulting PL lineshape is then a Bi-Lorentzian function.

4.3.3. Optical Analysis of Stress in Diamond Thin Films. Part I: Raman Analysis

In contrast to the high quality crystalline diamonds investigated by Davies, diamond films are known to contain a variety of defect types whose relative contribution to the stress needs to be determined. In addition to the silicon and nitrogen impurities present in diamond films (which are point-type defects), a high concentration of line and extended defects was found utilizing TEM spectroscopy [79, 87, 91, 92]. Yet another defect, the graphitic phase, appears as the most common defect in diamond films, although it has not yet been definitely classified as to being a point or a line defect. Hence an optical analysis as proposed by Stoneham is a potentially useful technique to classify the graphitic phase and to differentiate the contributions to the strain from each defect type.

Recently, the stress state in diamond thin films containing various concentrations of defects and impurities was investigated utilizing Raman as well as PL spectroscopy [15]. The following presents a summary of the analysis. Figure 4.3a shows the diamond and the graphitic Raman signals for four samples; Fig. 4.3b shows the high resolution normalized diamond Raman spectra. From the dependence of the Raman shift $\Delta\nu$ on the stress σ [10, 93] given by

$$Dn = n - n_0 = - as \qquad (4.5)$$

where ν_0 (~ 1332.3) is the Raman peak position of an unstressed diamond and α (~1.9 cm^{-1}/GPa) is the pressure coefficient, it was found that all of the diamond films exhibit a

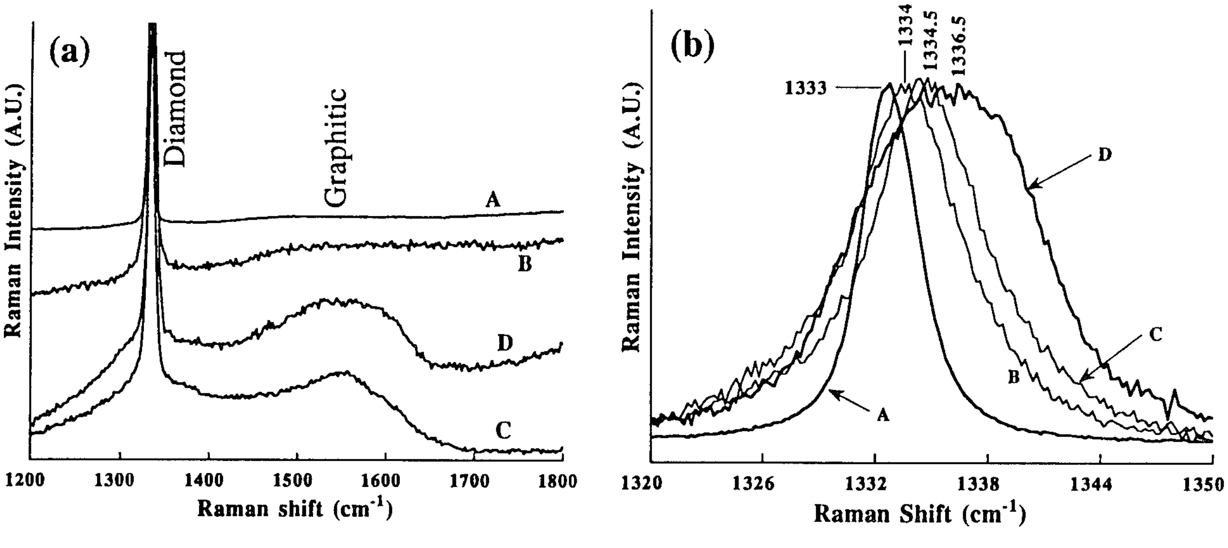

Figure 4.3 The Raman spectra of the diamond films: (a) showing the diamond and the graphitic signals, (b) The normalized high resolution Raman spectra of the diamond signal of the films. Sample A was grown in the controlled combustion chamber and is ~3μm thick, sample B was grown via the CVD method and is ~2 μm thick, samples C and D were prepared utilizing the hot filament growth method and the substrate coverage is ~80%. From Bergman *et al.* [15].

Table I. The Raman Characteristics of the Four Diamond Thin Films [15]

Sample	Diamond Position [cm^{-1}]	$I_{DIAMOND}/I_{GRAPHITIC}$	$\Delta\nu$ [cm^{-1}]	σ_{net} [GPa]
A	333.0	4.6	0.7	-0.37
B	334.0	1.8	1.7	-0.90
C	334.5	0.7	2.2	-1.16
D	336.5	0.6	4.2	-2.21

net compressive stress (σ_{net}). Table I lists the calculated stress values, as well as the Raman characteristics of the films obtained from Fig. 4.3. Next, the sources of stress in the diamond films were analyzed by identifying the stress components and estimating the contributions to the net stress, σ_{net}, in each of the diamond films. The observable σ_{net} is given by Eq. 4.6 in terms of the thermal stress, σ_{TH}, and the sum of the internal stresses σ_{IN} :

$$\sigma_{net} = \sigma_{TH} + \Sigma\sigma_{IN} \tag{4.6}$$

The thermal stress which arises from the difference in the thermal expansion coefficients of silicon and diamond is expected to be compressive in the growth temperature range of the films studied here [94]. The values of σ_{TH} were determined from the growth temperature and are listed in Table II. The total internal stress component $\Sigma\sigma_{IN}$ in the diamond film may be due to various sources such as impurities, structural defects such as dislocations, and interactions across grain boundaries. The interactions across grain boundaries, due to atomic attractive forces, have been reported to be the possible origin of the main intrinsic tensile stress, $\sigma_{IN,GB}$, in the diamond films [94, 95]. The $\sigma_{IN,GB}$, has been found to be inversely proportional to the average grain diameter, d, in a film [96]:

$$\sigma_{IN,GB} = [E\ (1 - \nu)]\ (\delta / d) \tag{4.7}$$

where δ=0.077 nm is the constrained relaxation of the lattice constant and E(1-ν)=1345 GPa is the biaxial Young's modulus of diamond. The average grain sizes for the A, B, C and D samples were ~ 3.5, 1, 1.5, and 2.5 μm respectively. The values of $\sigma_{IN,GB}$ as well as the values of the previous stress components found so far are listed in Table II.

From the results listed in Table II it may be concluded that the thermal stress and the stress due to the grain boundaries are not very significant, and that, after compensating for their contributions ($\sigma_{calculated}$), the samples still exhibit an appreciable excess of internal compressive stress.

Table II. The Experimental and the Calculated Stress Components of the Diamond Films [15]

Sample	σ_{net} [GPa]	σ_{TH} [GPa]		$\sigma_{IN,GB}$ [GPa]	$\sigma_{calculated}$ $=\sigma_{TH} + \sigma_{IN,GB}$	Internal Stress[GPa] $=\sigma_{net} - \sigma_{calculated}$
A	- 0.37	- 0.155	(1000°C)	+ 0.03	- 0.125	- 0.25
B	- 0.90	- 0.25	(750°C)	+ 0.104	- 0.146	- 0.75
C	- 1.16	- 0.23	(850°C)	+ 0.07	- 0.16	- 1.00
D	- 2.21	- 0.23	(850°C)	+ 0.042	- 0.188	- 2.02

To investigate the role of the graphitic phase as a source of internal stress in the thin diamond films, the relative graphitic concentration versus the internal stress was plotted. The graph is shown in Fig. 4.4, and for each sample the other observed non-graphitic impurities are listed. The correlation shown in Fig. 4.4 indicates that the graphitic phase may be a major contributor to the internal compressive stress but may not be the sole cause of the stress. The deviation from linearity is attributed to the internal stress exerted by the silicon and nitrogen impurities as well as possibly by structural defects.

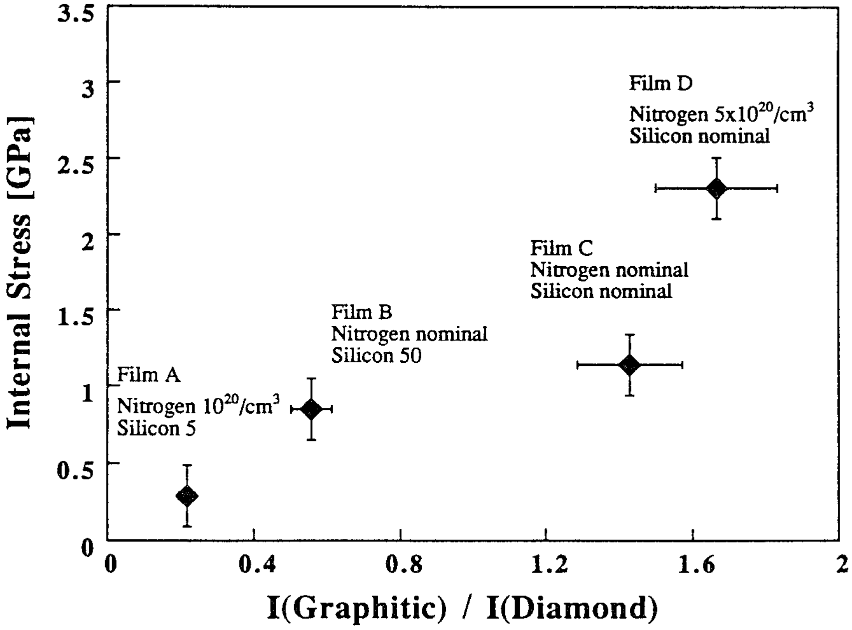

Figure 4.4 The correlation between the internal stress Δ and the graphitic phase Raman signal. Concentrations of the various impurities are also listed. The nitrogen concentration was obtained via SIMS while that of Silicon in arbitrary units was estimated from the ratio of the intensities of the silicon-PL and the diamond Raman. From Bergman *et al.* [15].

4.3.4. Optical Analysis of Stress in Diamond Thin Films, Part II: PL Analysis

In order to further investigate the stress state in the diamond films, PL lineshape analysis was carried out [15]. Figures 4.5a and 4.5b show the 2.154 eV PL bands of samples D and A respectively as well as the Lorentzian and Gaussian lineshape (of the same widths as the PL linewidths). It can be seen from the figures that both PL lineshapes exhibit a high degree of symmetry. In this respect the PL bands of the films are similar to the symmetric 2.154 eV PL lineshape of Ia crystalline diamond [72]. It can also be seen in Figs. 4.5a and 4.5b that the PL lineshape of sample D is mainly a Gaussian with a very small Lorentzian component and that

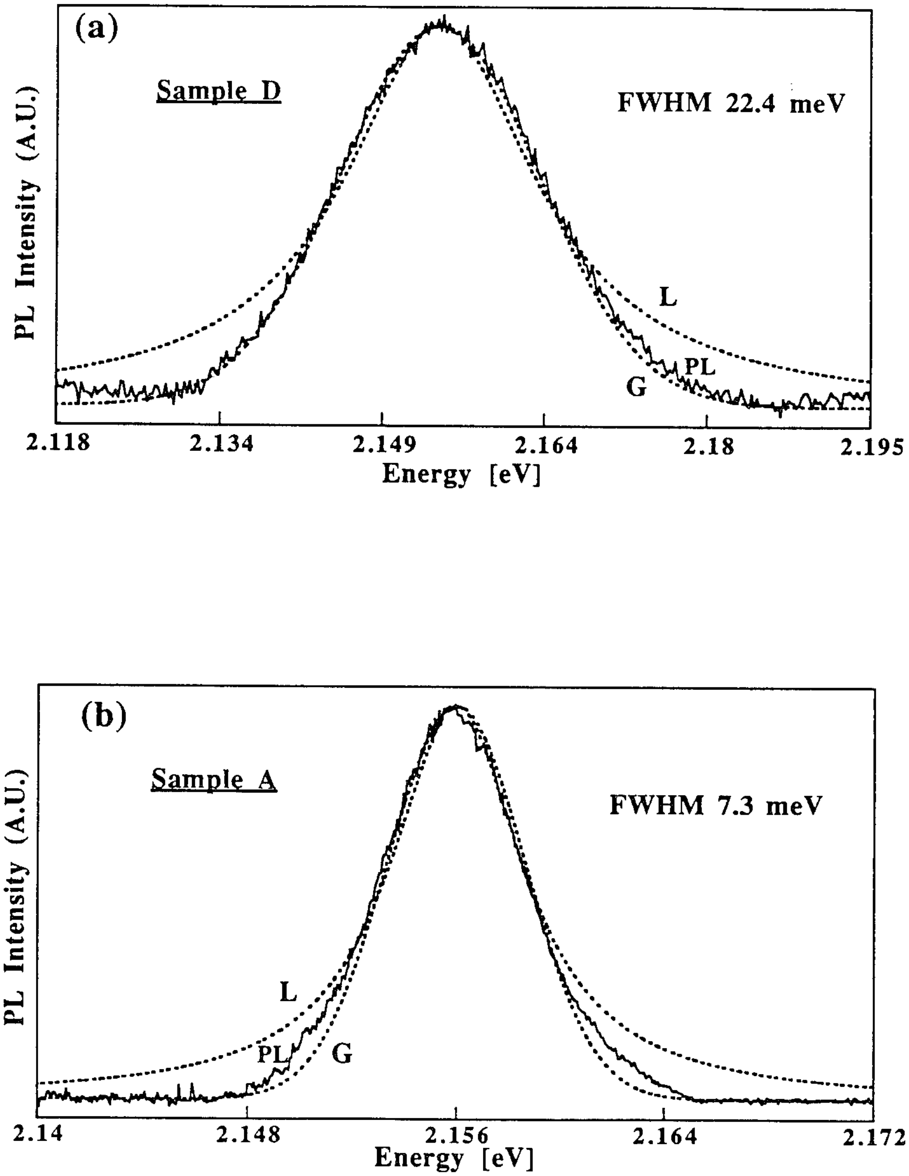

Figure 4.5 The Lorentzian (L) and the Gaussian (G) fits to the 2.154 eV nitrogen PL band of (a) sample D and (b) sample A. From Bergman *et al.* [15].

the lineshape of sample A lies between a Lorentzian and a Gaussian function. The relative linewidths of the Gaussian and Lorentzian components of each of the PL bands may be found by a deconvolution procedure and can be used to determine the respective stress contributions from line and point type defects. The following paragraphs outline the procedure. It has been demonstrated that the Voigt profile can be approximated by a linear combination of the Gaussian and the Lorentzian functions [97]:

$$I(\omega) / I_0 = [1 - W_L/W_V] \exp[-2.772 \{(\omega-\omega_0)/W_V\}^2] +$$

$$+ [W_L/W_V] \{1/(1+4((\omega-\omega_0)/W_V)^2)\} \tag{4.8}$$

where W_L and W_V are the Lorentzian and the Voigt linewidths respectively (to be determined). Once W_L and W_V have been determined from the curve fit of the given PL line to Eq. 4.8, the following relation between the Lorentzian and Gaussian linewidths [97]:

$$W_V = \left(\frac{W_L}{2}\right) + \sqrt{(W_L^2/4) + W_G^2} \tag{4.9}$$

is used to find the Gaussian linewidth component W_G.

Figure 4.6 shows that the PL line of the sample A (obtained from a high resolution PL spectrum) can be approximated well by Equation 4.8; from the curve fit and Eq. 4.9 the values of W_L and W_G were calculated to be 2.3 and 6.0 meV respectively. The ratio of $W_L/W_G=0.38$ implies that the Gaussian stress, which will be referred as S_G, is approximately 2.6 times greater than the Lorentzian stress S_L. The same analytical procedure was performed on the PL band of sample D and its results are presented in Figure 4.7. The values of W_L and W_G shown there are 3.2 and 20.8 meV respectively; hence the Gaussian stress in this sample is ~7 times greater than the Lorentzian stress.

Next, the assignment of stress values to the observed Gaussian and Lorentzian line-broadening components was performed as follows. It has been demonstrated that the total internal stress, S ($=S_L+S_G$), in a given diamond sample may be obtained from the linewidth W of a nitrogen PL band via the following approximation [12, 98]:

$$S \cong W / 10 \tag{4.10}$$

where S is in units of GPa and the linewidth W is in meV. Hence the stresses of samples A and D as obtained from the PL linewidths are ~ 0.73 and 2.24 GPa, respectively. These stress values are of a similar order of magnitude and consistent with the compressive stress values obtained previously from the Raman shift, implying that the Raman shift and the PL line broadening result from the same compressive stress sources. Combining the results calculated

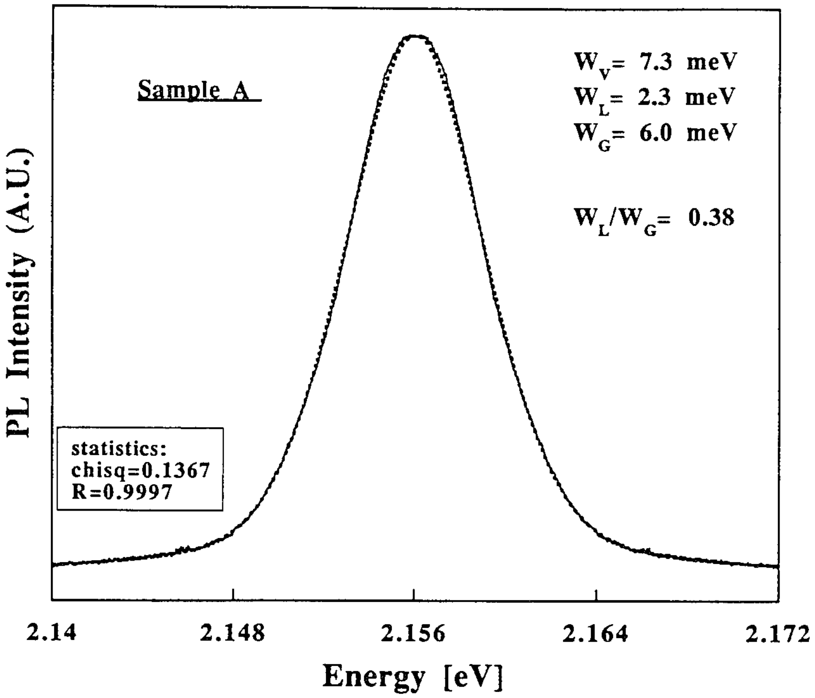

Figure 4.6 The high resolution spectrum of the 2.154 eV ZPL of sample A. The curve fit to the Voigt profile (Eq.4.8) is represented by the dashed line. In order to get a meaningful fit, a bilateral symmetric spectrum was derived by mirroring the side which exhibits the lowest background noise. From Bergman *et al.* [15].

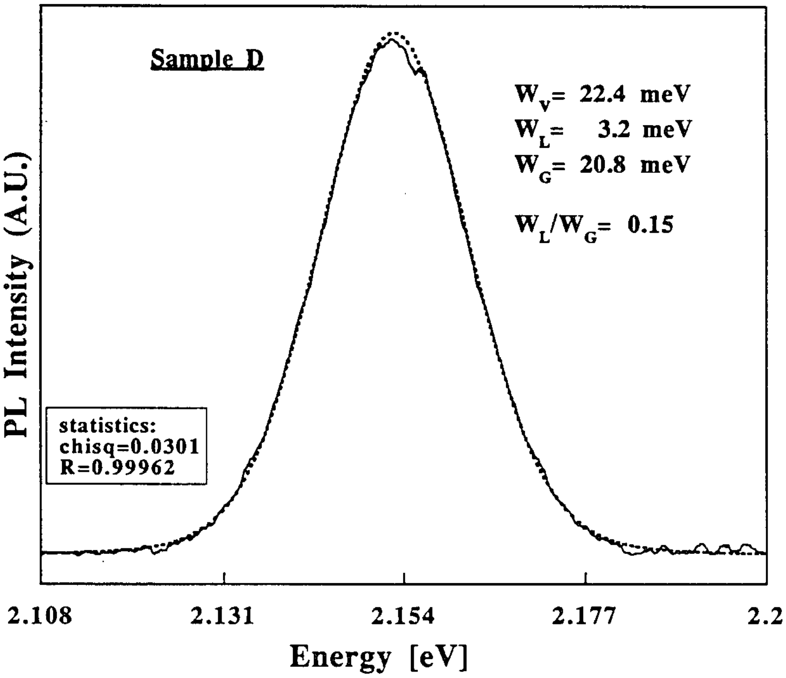

Figure 4.7 The high resolution spectrum of the 2.154 eV ZPL of sample D. The curve fit of the Voigt profile (Eq.4.8) is represented by the dashed line. From Bergman *et al.* [15].

via Eq. 4.10 for the S's with the previously calculated ratios W_L/W_G ($\equiv S_L/S_G$) it was found that for sample A the Lorentzian stress S_L is ~ 0.20 GPa and the Gaussian stress S_G is ~ 0.53 GPa, while for sample D S_L~0.29 GPa and S_G~1.95 GPa. Table III summarizes the above results for both samples.

Table III. The Linewidth of the 2.154 eV PL Nitrogen Bands and the Gaussian and Lorentzian Stress Components [15]

Sample	FWHM [meV]	Total Stress S [GPa]	S_G [GPa]	S_L [GPa]
A	7.3	0.73	0.53	0.20
D	22.4	2.24	1.95	0.29

According to the results listed in Table III, it was concluded that the samples exhibited mainly a Gaussian stress and to a much smaller degree a Lorentzian stress. Therefore the PL investigation indicated that line-type defects contribute far more to the stress existing in the diamond thin films than the point defects.

Based on the result, obtained from the Raman analysis, that the graphitic phase is a major contributor to the internal compressive stress, it was further concluded that the dominant Gaussian stress is mainly due to the graphitic phase. One implication of this finding is that the sp^2 bonding does not act as a point defect stress source but rather as a line or extended type defect .

4.3.5. Stress in Diamond Grit

Raman and PL spectroscopy have also been used to investigate the stress state in diamond grit. Synthetic diamond grit consists of 100 - 1000 μm size diamond crystallites which are grown by high-pressure high-temperature processes. In the studies by McCormick *et al.* [16, 99] the optical characteristics of different types of grit (i.e. prepared with different growth conditions) were correlated with the mechanical strength of the grit. The latter was measured in terms of the amount of force applied on the grit in order to initiate cracking, referred to as the crushing force. The following presents a short summary of the optical analyses of the diamond grit as described in [16, 99].

One of the main issues of the study was to ascertain whether there was a correlation between the optical centers and the strength of the crystals. The measurements attempted to correlate microscopic properties relating to the defect and impurity concentrations and configurations with macroscopic properties, namely strength. The issue is of relevance to synthetic diamond grit since impurities like nitrogen as well as vacancies can readily be incorporated (due to the extreme growth conditions) and strongly affect the mechanical properties of the small-volume crystallites.

In order to examine the influence of the nitrogen impurity on the strength of the grit, the relative abundance of the nitrogen optical centers of several different groups of grit were qualitatively inferred from the PL measurements. The measurements were performed with a microfocus system such that (111) faces of individual particles (crystals) could be examined. All measurements were obtained from surfaces in an unstrained area that was free of inclusions, cracks or other visible defects. The intensity of the 1.945 eV (N-V) PL spectra of several samples is presented in Figure 4.8. Here it should be noted that the PL experiments will only measure the optically active nitrogen centers (i.e. see section 4.1), and much of the nitrogen may actually be bonded in optically inactive configurations. Figure 4.9 presents a correlation between the PL intensity of the 1.945 eV PL (N-V) band and the crushing force. The correlation presented in the figure indicates a negative effect of the N-V centers on the strength of the diamond grit. However, when the 2.46 eV (H3) optical center, which consists of an N-V-N configuration, was correlated with the crushing force it was found that the H3 optical centers exert a positive influence on the strength of the diamond grit (Figure 4.10).

There have been many conflicting reports on the strengthening role of nitrogen; however, the above results are in accord with the suggestion of G. Bokii *et al.* [100] that a balance of the nitrogen forms and concentrations must be achieved in order to maximize the strength. Further investigation should be initiated to explain why some forms of nitrogen act as a strengthening agent while other forms do not.

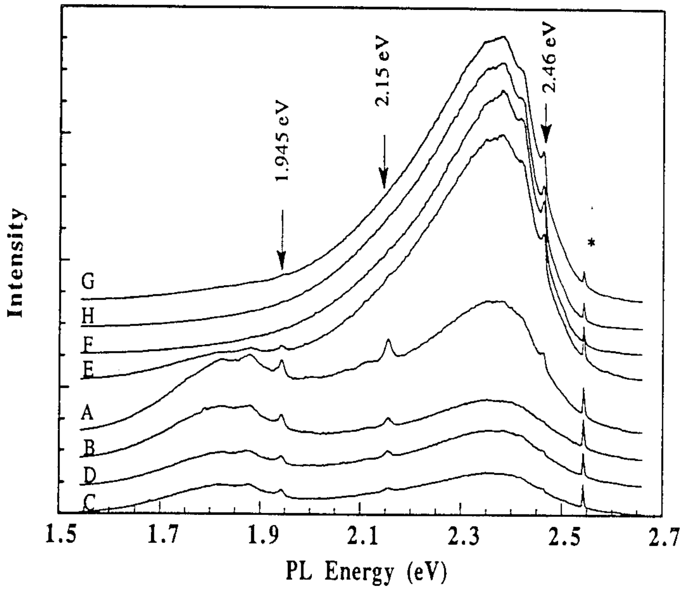

Figure 4.8. PL spectra of the various diamond grit samples. From McCormk *et al.* [16, 99].

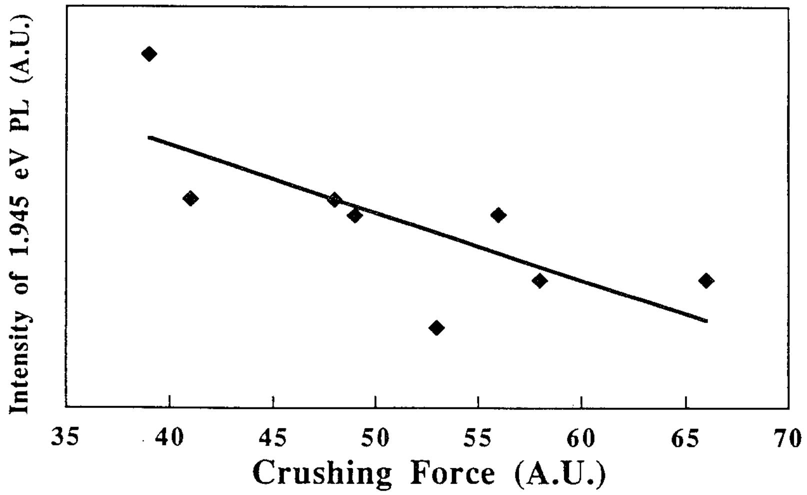

Figure 4.9 Correlation of the 1.945 eV PL integrated intensity with the crushing force. The PL intensity is normalized to the diamond Raman intensity. From McCormick [99].

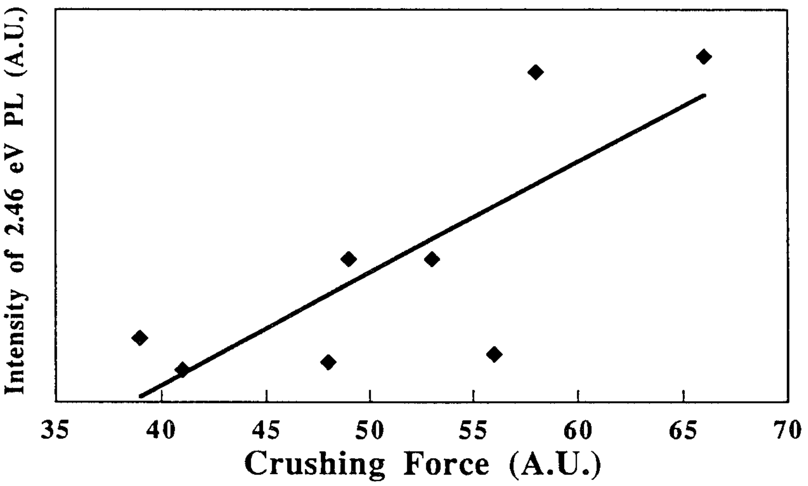

Figure 4.10 The correlation of the 2.46 PL normalized intensity with the crushing force. From McCormick [99].

The magnitude of the internal stress in the various grit samples was estimated using Equation 4.10 and the linewidth of the 1.945 eV PL band. It was found that the internal stress ranges between 0.5 to 1 GPa and exhibits a correlation with the crushing force as can be seen in Figure 4.11. The internal stress was attributed to the combined (and possibly correlated) effect of the various point and line defects as well as to macroscopic inclusions in the grit. Figure 4.12 presents photographs of characteristic defect-free and defective grit samples.

Annealing studies of the diamond grit have also been conducted by McCormick [99] and Webb *et al.* [101]. Both studies employed PL in an attempt to characterize the properties of the defect and impurity structures. Figure 4.13 compares the PL spectra of diamonds before and after annealing. The sample was annealed at high pressure high temperature (HPHT) conditions (60 kbar and 1200 ^{0}C respectively) for 1 hour. It can be seen in the figure that after annealing, the PL intensity of the H3 center and its vibronic sideband was somewhat diminished while the 2.154 and the 1.945 eV systems exhibit a considerable increase in intensity. Figure 4.14 presents the spectra of the grit samples before and after the low pressure high temperature (LPHT) anneal (i.e., at 1 atm and 1200 ^{o}C). As opposed to the HPHT, the LPHT anneal resulted in an increase in intensity of the H3 vibronic system. In addition, the study also noted changes in the strength of the diamonds depending on the annealing conditions.

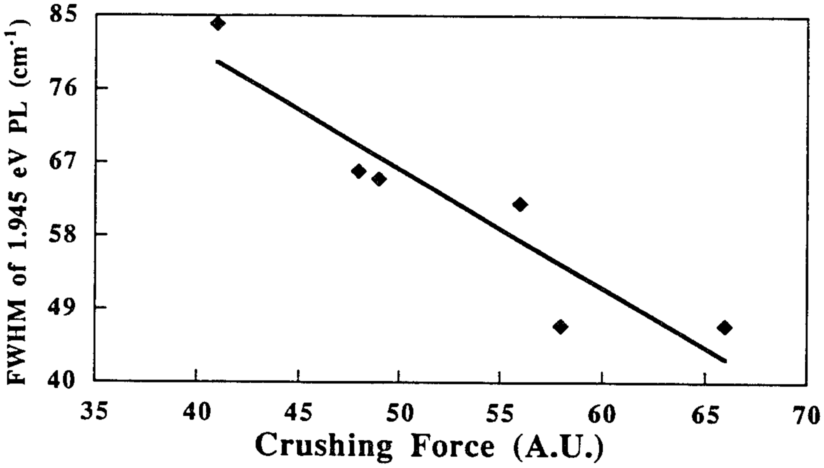

Figure 4.11 The internal stress (expressed in term of the FWHM of the 1.945 eV ZPL in units of cm^{-1}) of the diamond grit in correlation with the crushing force. From McCormick [99].

The large changes in the PL demonstrate the value of this technique in exploring how defects and microstructure are affected in processing environments. The observed PL changes may be indicative of the interactions of defects and impurities within the diamond. However, previous studies have suggested that high temperature annealing may involve plastic deformation and creation of vacancies that then enhance the PL of previously inactive nitrogen sites [12, 98].

5. The 1.68 eV Optical Center

5.1. Structure

A luminescence band with a zero-phonon line (ZPL) at approximately 1.68 eV, as shown in Fig. 5.1, has been reported to be present in the PL and CL spectra of many diamond films [15, 56, 57, 102-106]. Early studies have speculated that the 1.68 eV center may be attributed to the GR1 optical center which can be produced by radiation damage in natural and synthetic diamond and has been established to consist of a neutral vacancy [66]. This hypothesis

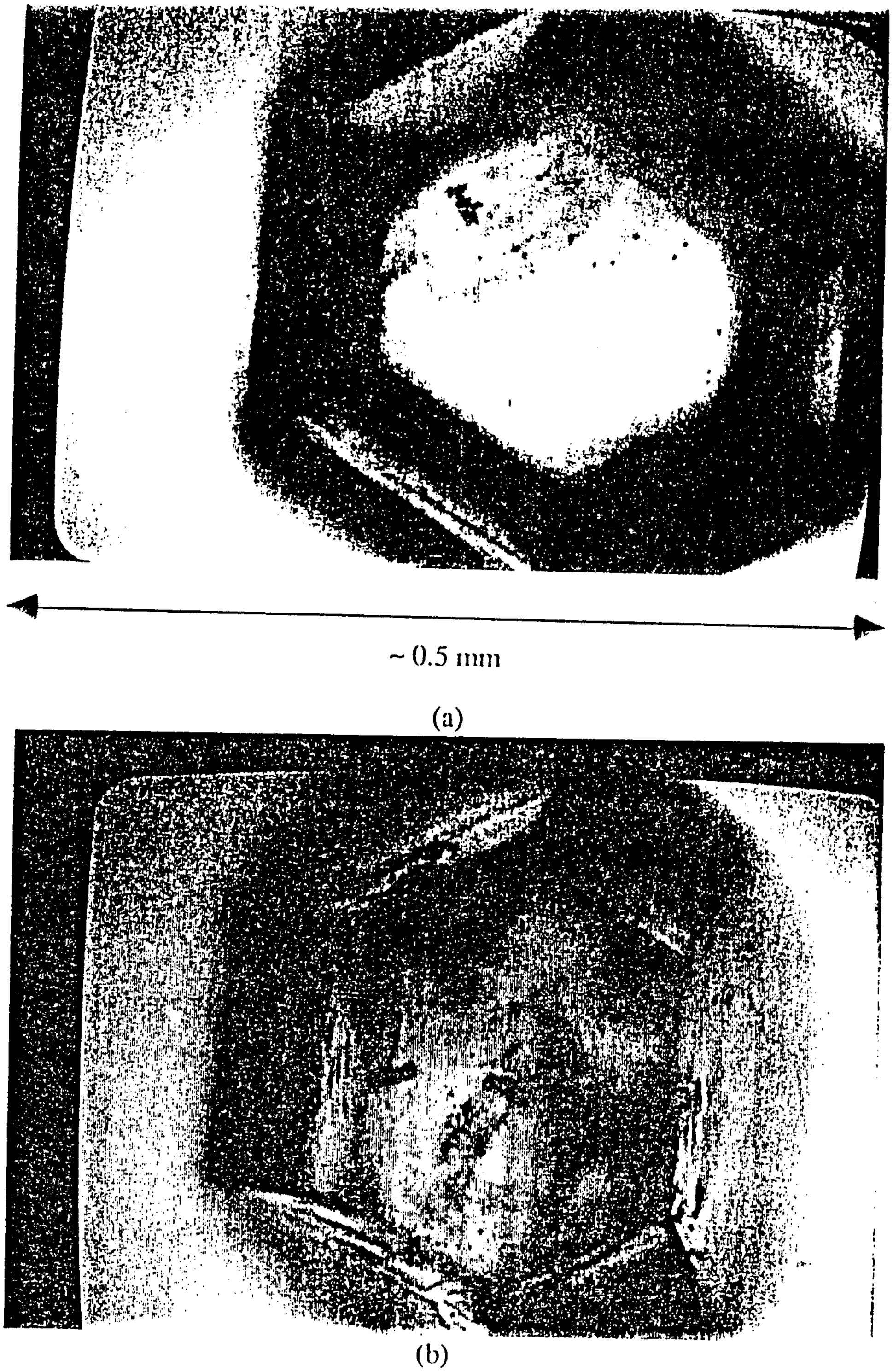

Figure 4.12 Characteristic pictures of the diamond grit. Sample (a) is relatively free of defects and sample (b) is filled with crack and inclusion content. From McCormick [99].

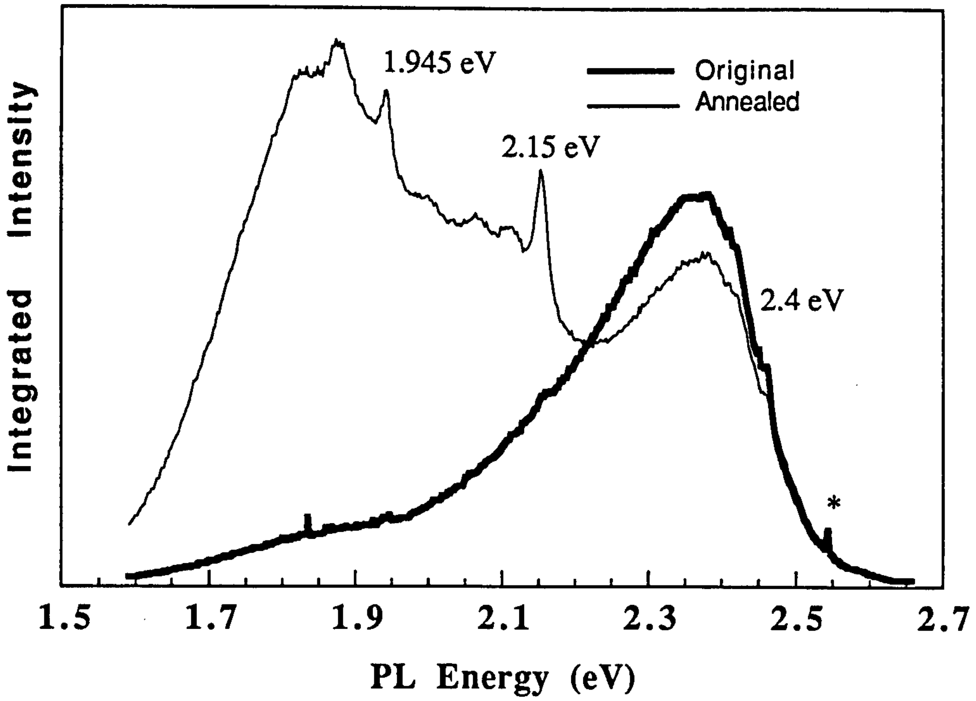

Figure 4.13 PL spectra of diamond grit before and after annealing at HPHT conditions. From Webb *et al.* [101].

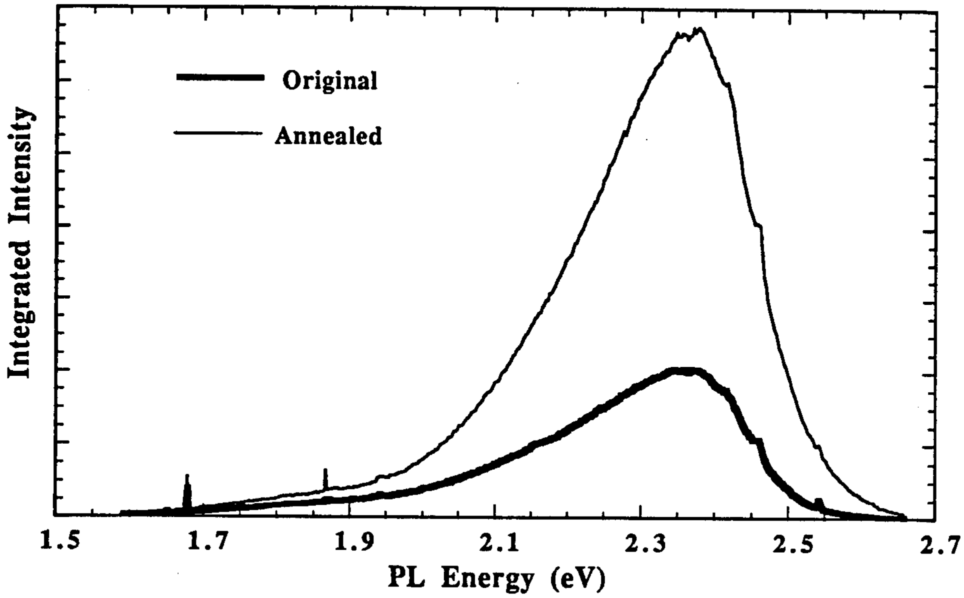

Figure 4.14 PL spectra of diamond grit before and after annealing at LPHT conditions. From Webb *et al.* [101].

originated from the observation that the GR1 in natural diamond gives rise to the closely proximate PL band with a ZPL at 1.673 eV. The small deviation between this PL line in natural diamond and that at 1.68 eV observed in diamond films had been attributed to the stress existing in the film which may interact with the GR1 center and shift the emission energy to 1.68 eV [58].

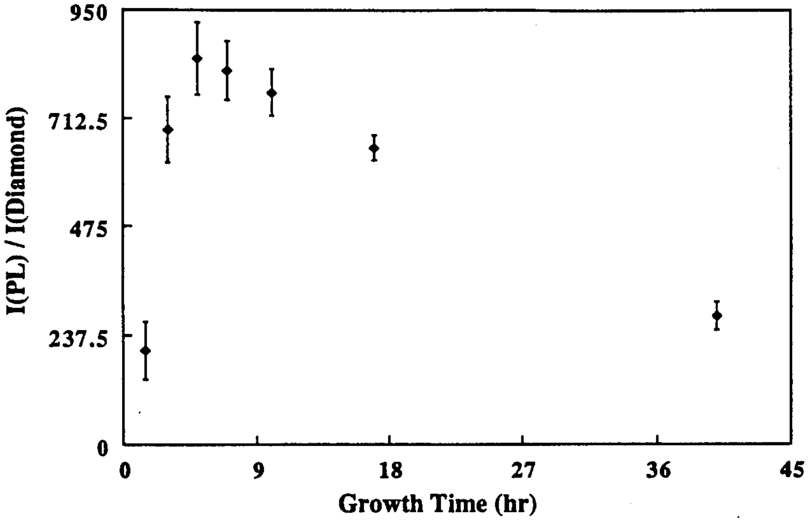

Figure 5.1 The characteristic room-temperature PL spectra of a diamond film showing the 1.68 eV band. The inset shows the Raman spectra of the film. From Bergman *et al.* [57].

Studies of silicon ion implantation into natural diamonds have been reported by Vavilov *et al.* [103] Clark *et al.* [107] and Collins *et al.* [65]. There it was found that, as a result of the silicon ion implantation, the 1.68 eV luminescence band appeared in the spectra. It was suggested by the researchers that the 1.68 eV band is due to a transition of a center involving a silicon atom [65, 103, 107]. Furthermore, the annealing behavior of the 1.68 eV center was found to be inconsistent with that of the GR1 center [107]. The intensity of the GR1 luminescence band diminishes significantly at ~ 700°C [108, 109], since the vacancy in diamond becomes mobile at this temperature, while the 1.68 eV band intensity was observed to increase [107].

In order to examine the influence of silicon incorporation in CVD diamond films, Badzian *et al.* [102] have conducted experiments in which diamond was deposited on a graphite substrate as well as others where a piece of a silicon wafer was placed on the graphitic substrate. The PL spectra obtained from the film grown in the latter experiments exhibited a significant increase in intensity of the 1.68 eV band relative to the intensity from the films grown on the bare graphite substrate. Other work [110] showed a direct correlation between the 1.68 eV luminescence intensity and the concentration of silicon in diamond films grown on silicon substrate. By now it is well established that the 1.68 eV optical band of diamond films is not associated with the neutral vacancy but rather has a silicon atom as one of its constituents.

A definitive model of the structure of the 1.68 eV center has yet to be formulated; however, two possible models have been suggested which are supported by experiment. From the observed quadratic dependence of the luminescence intensity on the silicon implantation dose, Vavilov *et al.* [103] have suggested that the center may contain two silicon atoms. Another suggested possible structure of the center is that of a silicon-vacancy pair [107, 111]: this structure was found to be consistent with the annealing behavior reported by Clark *et al.* [107]. In that work, the CVD diamond film was first irradiated by energetic electrons to induce local disorder and vacancies, and then annealed. The sharp increase in the 1.68 eV intensity band that was observed at the mobile vacancy temperature (700°C) led to the suggestion that the center involves a silicon atom and a vacancy.

5.2. Incorporation of the Silicon Impurity in Diamond Films: Time Dependence Study

The deposition of diamond films on silicon substrates is a widely used method and as such the silicon substrate becomes a principal potential source of silicon atom impurities in the diamond films [104, 112]. Other possible sources of silicon contaminant may be the walls of the growth chamber which in some reactors are made of quartz (SiO_2) [107], as well as residual silicon atoms which exist in the growth environment of the quartz and stainless steel chambers. Although the source of silicon contaminant depends, to large extent, on the specific growth system, the general mechanisms involved in the origin of the silicon impurity and its dynamic incorporation into the diamond film is an important topic and has been investigated by several researchers [57, 104, 107, 112].

The formation of the 1.68 eV centers in CVD diamond film deposited on silicon substrate as a function of growth time has been the subject of investigation [57]. In this study, the PL integrated intensity of the 1.68 eV line was calculated and normalized to the diamond integrated Raman line for the consecutive growth times (1.5, 3, 5, 7, 10, 17 and 40 hour) of a redeposited diamond sample. The results shown in Figure 5.2 indicate an initial increase of the 1.68 eV relative intensity until a maximum is reached at about 8 hours; thereafter the relative PL intensity is seen to decrease with increasing growth time. The SEM images of this sample shown in Figure 5.3 reveal that initially the film consists of isolated diamond particles; after ~8 hours the diamond particles start to coalesce, forming grain boundaries until most of the Si substrate is covered by the growth. A possible mechanism for the effect shown in Figure 5.2 is that etching of the Si substrate by the plasma releases Si atoms in the gas phase and allows them to become incorporated into the growing diamond film. In the early stages when the nucleation and growth of the isolated particles take place, the probability of creating the 1.68 eV centers is high since the Si substrate is almost entirely exposed to the plasma. As the diamond nuclei continue to grow in an isolated fashion, the concentration of the defect centers increases. At deposition times longer than 8 to 10 hours, less of the Si substrate is exposed to the plasma, resulting in a reduced concentration of the 1.68 eV defect centers.

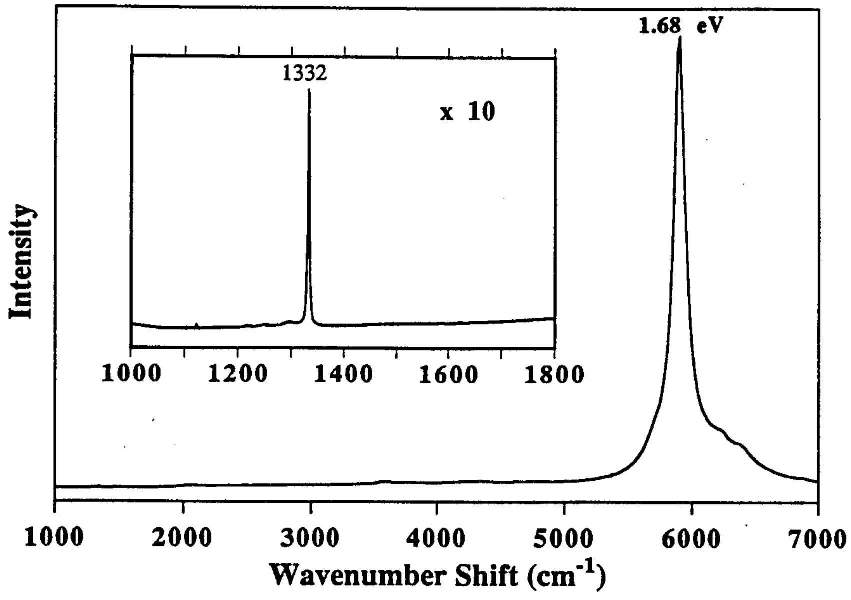

Figure 5.2 The relative integrated PL intensity of the 1.68 eV band as a function of deposition time. The highest intensity occurs at ~ 7 h. From Bergman *et al.* [57].

Cathodoluminescence studies carried out by Robins *et al.* [112] on the formation of the 1.68 eV center in CVD diamonds have resulted in a time dependence behavior similar to that presented in Fig. 5.2. The observed time dependence of the incorporation of the optical centers at early stages of growth implies that the spatial distribution of the centers is concentrated at the interface of the silicon substrate and the diamond film.

5.3. The Vibronic System and Temperature Dependence of the 1.68 eV Center

As discussed in the previous sections, optical centers, when excited, can interact with the lattice vibrations through various mechanisms. One type of electron-lattice interaction is energy transfer from a photoexcited optical center to the phonons which results in a vibronic side band spectra relative to the zero-phonon line (ZPL) band. By calculating the energy difference between the side band and the ZPL peaks, the energy of the specific phonon involved in the interaction may be obtained. Figure 5.4 shows the PL emission spectrum of the 1.68 eV optical line and its vibronic side bands for a CVD diamond film as reported by Feng *et al.* [106]. Feng *et al.* interpreted the spectrum presented in Figure 5.4 as consisting of a zero-phonon line at 1.681 eV (labeled Z) and its vibronic side bands. Two of the dominant side bands, the 1.639 eV and the 1.616 eV (labeled A and B respectively) which correspond to ~42 and ~65 meV phonons, were attributed to a local vibrational mode of the center and to a transverse acoustic mode (TA) of the diamond lattice respectively.

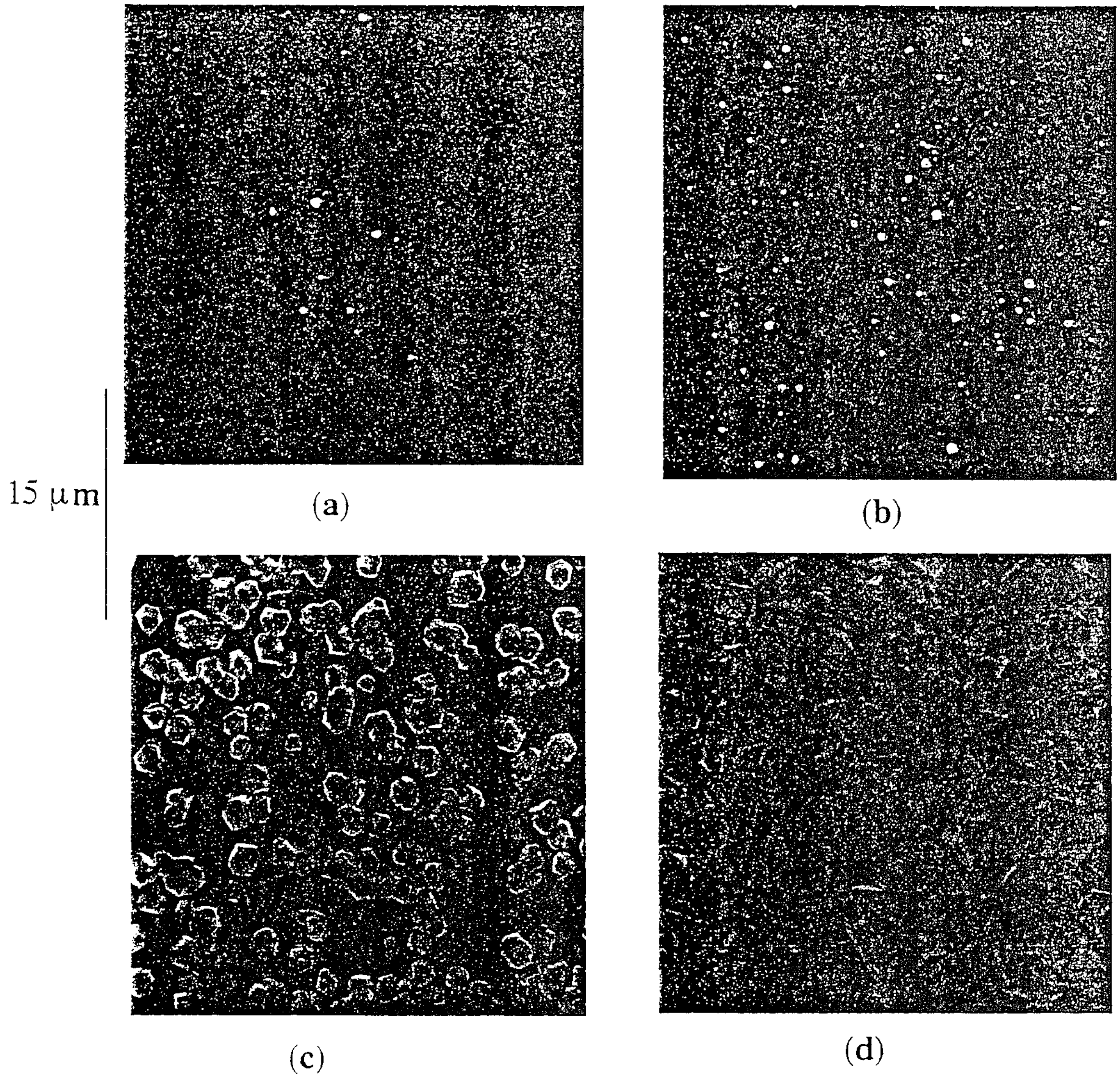

Figure 5.3 The SEM micrographs of the diamond sample at (a) 1.5, (b) 3, (c) 10, and (d) 40 h of deposition time. From Bergman *et al.* [57].

According to the model of electron-lattice interaction [32], the total band intensity which includes the zero-phonon line and its vibronic sideband is expected to be independent of temperature. As the temperature increases, the zero-phonon line intensity decreases, and the vibronic band intensity is expected to increase proportionally so as to keep the total intensity constant with temperature. Figure 5.5 shows the 1.68 eV PL band for various temperatures as reported in [56]. It can be observed in the figure that the conservation of the total intensity of the ZPL and its sidebands does not hold as a function of temperature, indicating a weak electron-lattice interaction and the existence of another nonradiative channel of the 1.68 eV luminescence.

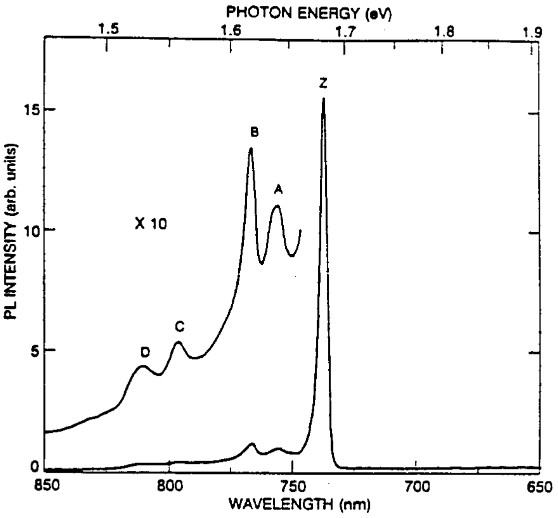

Figure 5.4 The 1.681 eV PL emission spectrum at 10 K of a diamond film. Peaks A-D are vibronics related to the 1.681 eV ZPL labeled Z. From Feng *et al.* [106].

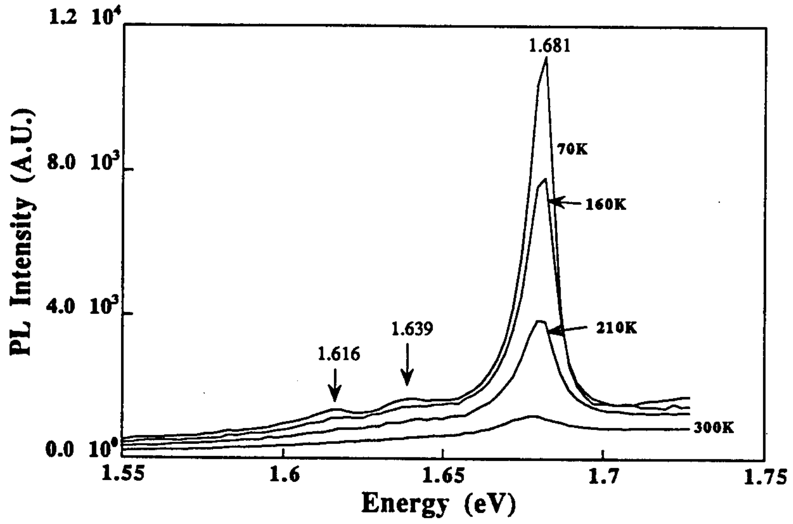

Figure 5.5 The 1.681 eV PL band and its vibronic side bands of diamond film at various temperatures. From Bergman *et al.* [56].

Another possible mechanism through which the PL intensity of a ZPL can be quenched is known as the Boltzmann process. In this process there exists an activation energy E_A associated with a certain nonradiative decay channel in the crystal which acts to decrease the PL intensity according to the relation

$$\frac{I_0}{I(T)} - 1 \sim \exp\left(\frac{-E_A}{k_B T}\right) \qquad (5.1)$$

where I(T) is the PL intensity at a given temperature and I_0 is the intensity for the temperature approaching absolute zero. Figure 5.6 shows that the sampled 1.68 eV PL intensity can be closely fitted by Eq. 5.1, with an activation energy E_A=90 meV(±10 meV) [56]. The Boltzmann process was also reported to be the dominant luminescence quenching mechanism by Feng *et al.* [106] with E_A~70 meV and by Collins *et al.* [111] with E_A=56 meV. The different values of the activation energy may be due to experimental error, but one can not exclude the possibility that different activation energies are due to differences in film quality. At present the identity of the nonradiative channel is not known; nonetheless, in light of the above reported findings it can be speculated to be a defect or an impurity rather than a vibronic interaction.

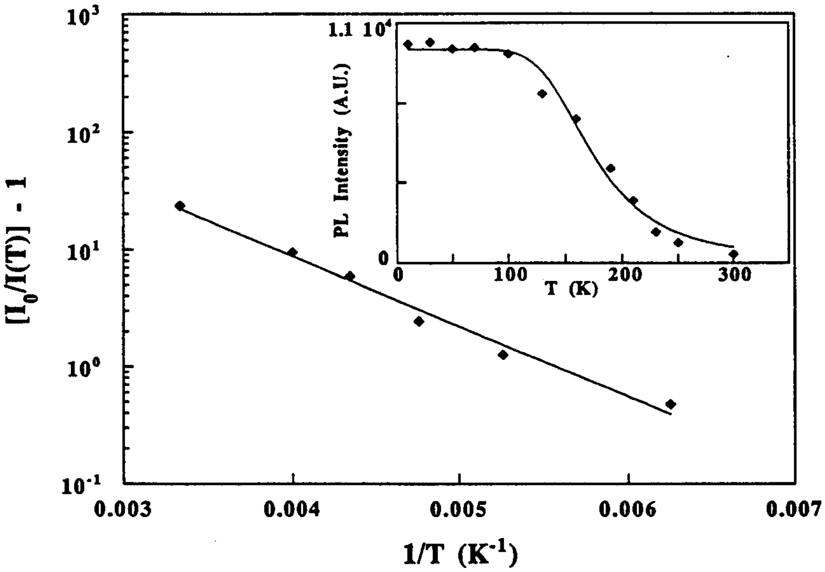

Figure 5.6 The functional behavior of the 1.681 eV PL intensity vs 1/T. The inset shows the PL intensity vs temperature. From Bergman *et al.* [56].

Complementary to photoluminescence techniques, the absorption and cathodoluminescence characteristics of the 1.68 eV optical system in CVD diamond films were recently investigated by Collins *et al.* [113]. The spectrum they obtained is shown in Fig. 5.7, and it can be seen that the center absorbs and emits at the same energy. This finding may be indicative of a relatively small vibronic interaction and is consistent with the lack of conservation of intensity of the vibronic center observed in [56].

6. Concluding Remarks

Raman and luminescence spectroscopy have become effective and well established techniques for the characterization of diamond films. This chapter has presented a review of the various Raman and luminescence techniques employed in the study of defects and impurities in diamond films.

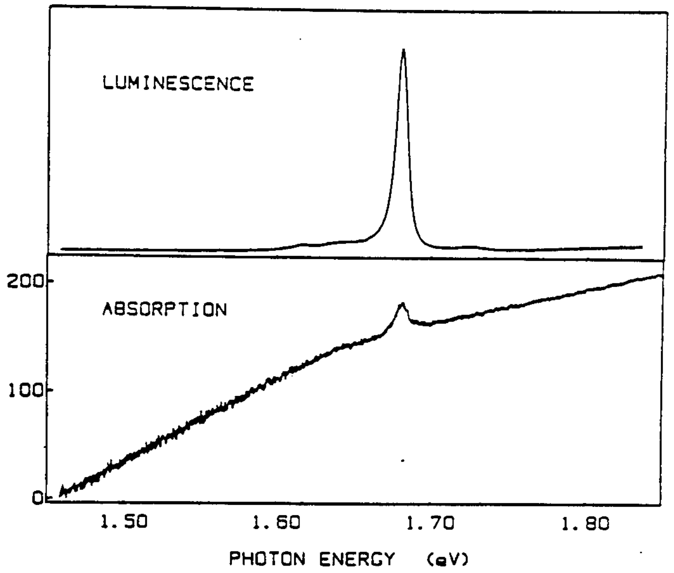

Figure 5.7 Cathodoluminescence and absorption spectra of the 1.681 ZPL of diamond film. The sample temperature was 77K for both. From Collins *et al.* [113].

One of the main applications of Raman spectroscopy is the identification of the sp^2-graphitic and sp^3-diamond phases which may coexist in a diamond film. Moreover, the relative concentrations of the two phases, a measure of the film purity, may be calculated via the Raman intensities.

Raman together with PL spectroscopy may also be utilized as complementary optical characterization techniques in order to investigate the stress state of a diamond film. When both techniques have been employed in the investigation of the stress in thin (< 3 μm) films it was found that the internal stress is compressive and is due mainly to extended and line type defects, in particular the graphitic phase. The source of the internal stress in high quality natural diamond crystals, in contrast, is due to point defects consisting of nitrogen impurities of the A-aggregate form. In addition to the investigation of point-like optical centers, cathodoluminescence spectroscopy has been proven to be useful also in the study of line type defects: the presence of dislocations in diamond, bulk as well as film, may be inferred from the occurrence of the blue band-A (~2.8 eV) luminescence.

Other significant results obtained via Raman and luminescence spectroscopy of diamond films are: (a) the diamond Raman lineshape is symmetric and can be approximated by a Lorentzian function. This result excludes the phonon confinement as the primary mechanism of line broadening. The mechanism proposed for the Raman line broadening is the phonon scattering at impurities and defects. (b) The broadband PL (~2 eV) is due to optical transitions of in-gap states which in turn are attributed to a disordered form of sp^2 type bonding. (c) The 1.681 eV luminescence band is attributed to an optical center containing silicon atom(s) and, possibly, a vacancy. In the case of diamond grown on a silicon substrate, most of the 1.681 eV centers reside near the silicon/diamond interface. This optical center luminesces and absorbs at the same energy, has a very weak vibronic interaction, and exhibits Boltzmann quenching with an activation energy of ~70 meV.

Among the many issues of interest which bear further investigation are the donor-acceptor recombination mechanism as an origin to the band-A luminescence, the structure and symmetry of the 1.681 eV optical center, and the spatial configurations (cluster size and dimensionality) of the graphitic phase, in particular the configurations which are responsible for the stress and for the broadband luminescence.

Acknowledgements

The authors gratefully acknowledge Alan T. Collins, Terri McCormick, and Peter Mills for their contribution. We also acknowledge the support of the Office of Naval Research.

References

1. K. V. Ravi, Materials Science and Engineering B **19**, 203-27 (1993).
2. J. E. Field (ed.), *The Properties of Natural and Synthetic Diamond* (Academic Press, New York, 1992).
3. G. Davies (ed.), *Properties and Growth of Diamond* (INSPEC, Institute of Electrical Engineers, London, 1994).
4. G. E. McGuire, in *Semiconductor Materials and Process Technology Handbook*, G. E. McGuire (ed.) (Noyes, New Jersey, 1987).
5. L. H. Robins, E. N. Farabaugh, and A. Feldman, *SPIE Vol.1325 Diamond Optics III* (1990), pp. 130.
6. E. S. Etz, E. N. Farabaugh, A. Feldman, and L. H. Robins, *SPIE Vol.969 Diamond Optics* (1988), pp. 86.
7. D. S. Knight, and W. B. White, *SPIE Vol.1055 Raman Scattering, Luminescence, and Spectroscopic Instrumentation in Technology* (1989), pp. 144.
8. R. J. Nemanich, J. T. Glass, G. Lucovsky, and R. E. Shroder, J. Vac. Sci. Technol. A **6**, 1783 (1988).
9. R. E. Shroder, R. J. Nemanich, and J. T. Glass, Phys. Rev. B **41**, 3738-45 (1990).
10. S. K. Sharma, H. K. Mao, P. M. Bell, and J. A. Xu, J. Raman Spec. **16**, 350 (1985).
11. J. W. Ager, and M. D. Drory, Phys. Rev. B **48**, 2601 (1993).
12. T. Evans, S. T. Davey, and S. H. Robertson, J. Materials Science **19**, 2405 (1984).
13. M. Yoshikawa, *et al.*, Appl. Phys. Lett. **57**, 428 (1990).
14. M. Yoshikawa, *et al.*, Appl. Phys. Lett. **55**, 2608 (1989).
15. L. Bergman, and R. J. Nemanich, J. Appl. Phys **78**, 6709-6719 (1995).
16. T. L. McCormick, W. E. Jackson, and R. J. Nemanich, C. L. Renschlers (ed.), *MRS Symposium Proc. Novel Forms of Carbon II* (1994), vol. 349, pp. 445.
17. F. H. Pollak, in *Analytical Raman Spectroscopy*, J. G. Grasselli, and B. J. Bulkin (ed.) (John Wiley and Sons, New York, 1991) pp. 137.
18. B. J. Bulkin, in *Analytical Raman Spectroscopy*, J. G. Grasselli, and B. J. Bulkin (ed.) (John Wiley and Sons, New York, 1991) pp. 1.
19. M. Cardona, *SPIE Vol.822 Raman and Luminescence Spectroscopy in Technology* (1987), pp. 2.
20. S. P. S. Porto, in *Light Scattering Spectra of solids*, G. B. Wright (ed.) (New York, 1969) pp. 1.
21. R. J. Nemanich, *Mat. Res. Soc. Symp. Proc.* (1986), vol. 69, pp. 23.

22. M. Cardona, in *Light Scattering in Solids I*, M. Cardona (ed.) (Springer-Verlag, New York, 1983) pp. 1.
23. A. Pinczuk, and E. Burstein, in *Light Scattering in Solids I*, M. Cardona (ed.) (Springer-Verlag, New York, 1983) pp. 23.
24. D. A. Long, *Raman Spectroscopy* (McGraw-Hill, New York, 1977).
25. R. Loudon, Proc. Roy. Soc. A **275**, 218 (1963).
26. R. Loudon, J. Phys. **26**, 677 (1964).
27. B. Di Bartolo, *Optical Interactions in Solids* (J. Wiley & Sons, Inc., New York, 1969).
28. W. J. Borer, S. S. Mitra, and K. V. Namjoshi, Solid State Comm. **9**, 1377 (1971).
29. R. J. Nemanich, S. A. Solin, and R. M. Martin, Phys. Rev. B **23**, 6348-56 (1981).
30. M. Gershenzon, in *Semiconductors and Semimetals*, R. K. Willardson, and A. C. Beer (ed.) (Academic Press, New York, 1966), vol. 2, pp. 289.
31. D. Curie, *Luminescence in Crystals* (John Wiley and Sons, 1963).
32. B. Henderson, and G. F. Imbusch, *Optical Spectroscopy of Inorganic Solids* (Clarendon Press, Oxford, 1989).
33. J. M. Hollas, *Modern Spectroscopy* (John Wiley and Sons, New York, 1992).
34. S. Matsumato, Y. Sato, M. Tsutsumi, and N. Setaka, J. Mater. Sci. **17**, 3106 (1982).
35. A. Sawabe, and T. Inuzuka, Thin Solid Films **137**, 89 (1986).
36. Y. Hirose, and Y. Terasawa, Jpn. J. Appl. Phys **25**, L519 (1986).
37. C. B. Zarowin, N. Venkataramanan, and R. R. Pool, Appl. Phys. Lett. **48**, 759 (1986).
38. V. Natarajan, J. D. Lamb, J. A. Woollam, D. C. Liu, and D. A. Gulino, J. Vac. Sci. Technol. A **3**, 681 (1985).
39. T. Mori, and Y. Namba, J. Vac. Sci. Technol. A **1**, 23 (1983).
40. J. C. Angus, and F. J. Jansen, J. Vac. Sci. Technol. A **6**, 1778 (1988).
41. R. C. Hyer, M. Green, and S. C. Sharma, Phys. Rev. B **49**, 14573 (1994).
42. D. S. Knight, and W. B. White, J. Mater. Res. **4**, 385 (1989).
43. K. Kobashi, K. Nishimura, Y. Kawate, and T. Horiuchi, Phys. Rev. B **38**, 4067 (1988).
44. S. A. Solin, and A. K. Ramdas, Phys. Rev. B **1**, 1687 (1970).
45. R. J. Nemanich, and S. A. Solin, Phys. Rev. B **20**, 392-401 (1979).
46. A. R. Ubbelohode, and F. A. Lewis, *Graphite and its Crystal Compounds* (Clarendon, Oxford, 1960).
47. S. A. Solin, and R. J. Kobliska, *Amorphous and Liquid Semiconductors* , J. Stuke (ed.) (Taylor Francis, London, 1974).
48. N. Wada, and S. A. Solin, Physica B **105**, 353-356 (1981).
49. J. Robertson, Advances In Physics **35**, 317 (1986).
50. J. Robertson, and E. P. O'Reilly, Phys. Rev. B **35**, 2946 (1987).
51. J. Robertson, Diamond and Related Materials **4**, 297 (1995).
52. J. W. Ager, D. K. Veirs, and G. M. Rosenblatt, Phys. Rev. B **43**, 6491-99 (1991).
53. I. H. Campbell, and P. M. Fauchet, Solid State Comm. **58**, 739 (1986).
54. P. M. Fauchet, and I. H. Campbell, Critical Reviews in Solid State and Materials Sciences **14**, S79-101 (1988).
55. R. Tubino, and J. L. Birman, Phys. Rev. B **15**, 5843 (1977).
56. L. Bergman, M. T. McClure, J. T. Glass, and R. J. Nemanich, J. Appl. Phys. **76**, 3020-27 (1994).
57. L. Bergman, B. R. Stoner, K. F. Turner, J. T. Glass, and R. J. Nemanich, J. Appl. Phys. **73**, 3951-57 (1993).
58. J. J.A. Freitas, J. E. Butler, and U. Strom, J. Mater. Res. **5**, 2502 (1990).
59. A. T. Collins, and S. C. Lawson, J. Phys.: Condens. Matter. **1**, 6929 (1989).
60. G. Davies, and M. F. Hamer, Proc. R. Soc. Lond. A. **348**, 285 (1976).
61. M. E. Pereira, M. I. B. Jorge, and M. F. Thomaz, J. Phys. C: Solid State Phys. **19**, 1009 (1986).

62. M. H. Nazare, M. I. B. Jorge, and M. F. Thomaz, J. Phys. C: Solid State Physics **18**, 2371 (1984).
63. R. C. Fang, J. Lumin. **48/49**, 631 (1991).
64. N. F. Mott, and E. A. Davis, *Electronic Processes in Non-Crystalline Materials* (Clarendon Press, Oxford, 1979).
65. A. T. Collins, M. Kamo, and Y. Sato, J. Mater. Res. **5**, 2507-13 (1990).
66. G. Davies, in *Chemistry and Physics of Carbon*, P. L. Walker, and P. A. Thrower (ed.) (Decker, New York, 1977), vol. 13, pp. 2.
67. G. Davies, Rep. Prog. Phys. **44**, 787 (1981).
68. R. A. Street, Advances In Physics **30**, 593 (1981).
69. T. Dallas, S. Gangopadhyay, S. Yi, and M. Holtz, *Applications of Diamond Films and Related Materials:Third International Conference* , A. Feldman, Y. Tzeng, W. A. Yarbrough, M. Yoshikawa, and M. Murakawa (ed.) (NIST Special Publication 885, USA, 1995).
70. S. Gangopadhyay, private Communication , (1995).
71. A. T. Collins, Diamond and Related Materials **1**, 457-469 (1992).
72. G. Davies, J. Phys. C: Solid State Phys. **3**, 2474 (1970).
73. G. Davies, Nature **228**, 758 (1970).
74. G. Davies, J. Phys. C: Solid State Phys. **9**, L537 (1976).
75. J. Walker, Rep. Prog. Phys. **42**, 1605 (1979).
76. C. D. Clark, and C. A. Norris, J. Physics C: Solid State Phys. **4**, 2223 (1971).
77. G. Davies, J. Phys. C: Solid State Phys. **12**, 2551 (1979).
78. L. H. Robins, L. P. Cook, E. N. Farabaugh, and A. Feldman, Phys. Rev. B **39**, 13367-77 (1989).
79. R. J. Graham, Mat. Res. Soc. Symp. Proc. Vol. **242**, 97 (1992).
80. R. J. Graham, and K. V. Ravi, Appl. Phys. Lett. **60**, 1310 (1992).
81. A. T. Collins, J. Phys. C: Solid St. Phys. **13**, 2641 (1980).
82. P. J. Dean, Phys. Rev. A **139**, 558 (1965).
83. A. T. Collins, M. Kamo, and Y. Sato, J. Phys.: Condens. Matter **1**, 4029 (1989).
84. A. A. Gippius, A. M. Zaitsev, and V. S. Vavilov, Sov. Phys. Semicond. **16**, 256 (1982).
85. S. J. Pennycook, L. M. Brown, and A. J. Craven, Phil. Mag. A **41**, 589 (1980).
86. N. Yamamoto, J. C. H. Spence, and D. Fathy, Phil. Mag. B **49**, 609 (1984).
87. R. J. Graham, T. D. Moustakas, and M. M. Disko, J. Appl. Phys. **69**, 3212 (1991).
88. A. E. Hughes, J. Phys. Chem. Solids **29**, 1461 (1968).
89. A. M. Stoneham, Proc. phys. Soc. **89**, 909 (1966).
90. A. M. Stoneham, Rev. of modern Phys. **41**, 82 (1969).
91. W. Zhu, A. R. Badzian, and R. Messier, J. Mater. Res. **4**, 659-63 (1989).
92. B. E. Williams, J. T. Glass, R. F. Davis, K. Kobashi, and T. Horiuchi, J. Vac. Sci. Technol. A **6**, 1819-20 (1988).
93. M. H. Grimsditch, E. Anastassakis, and M. Cardona, Phys. Rev. B **18**, 901 (1978).
94. H. Windischmann, G. F. Epps, Y. Cong, and R. W. Collins, J. Appl. Phys. **69**, 2231-37 (1991).
95. J. A. Baglio, B. C. Farnsworth, S. Hankin, G. Hamill, and D. O'Neil, Thin Solid Films **212**, 180 (1992).
96. F. A. Doljack, and R. W. Hoffman, Thin Solid Films **12**, 71 (1972).
97. E. E. Whiting, J. Quant. Spectrosc. Radiat. Transfer. **8**, 1379 (1968).
98. A. T. Collins, and S. H. Robertson, J. Mat. Sci. Lett. **4**, 681 (1985).
99. T. L. McCormick, *Master Thesis* (North Carolina State University, 1994).
100. G. B. Bokii, N. F. Kirova, and V. I. Nepsha, Sov. Phys. Dokl. **24**, 83 (1979).
101. S. W. Webb, and W. E. Jackson, J. Mater. Res. **10**, 1700 (1995).
102. A. R. Badzian, T. Badzian, R. Roy, R. Messier, and K. E. Spear, Mat. Res. Bull. **23**, 531-48 (1988).
103. V. S. Vavilov, *et al.*, Sov. Phys. Semicond. **14**, 1078 (1980).
104. J. Ruan, W. J. Choyke, and W. D. Partlow, Appl. Phys. Lett. **58**, 295 (1991).

105. J. Ruan, W. J. Choyke, and W. D. Partlow, J. Appl. Phys. **69**, 6632-36 (1991).
106. T. Feng, and B. D. Schwartz, J. Appl. Phys. **73**, 1415 (1993).
107. C. D. Clark, and C. B. Dickerson, Surface and Coating Technology **47**, 336 (1991).
108. C. D. Clark, and E. W. J. Mitchell, J. W. Corbett, and G. D. Watkinss (ed.), *Proc. 1970 Conf. Radiation Damage in Semiconductors* (Gordon and Breach, London, 1971), pp. 257.
109. A. T. Collins, Inst. Phys. Conf. Ser. **31**, (1977).
110. B. G. Yacobi, A. R. Badzian, and T. Badzian, J. Appl. Phys. **69**, 1643 (1991).
111. A. T. Collins, L. Allers, C. J. H. Wort, and G. A. Scarsbrook, Diamond and Related Materials **3**, 932 (1994).
112. L. H. Robins, E. N. Farabaugh, A. Feldman, and L. P. Cook, Phys. Rev. B **43**, 9102 (1991).
113. A. T. Collins, M. Kamo, and Y. Sato, *Proc. Mat. Res. Soc. Symp.* (1990), vol. 162, pp. 225-230.

V. Distribution List

Mr. Max Yoder Office of Naval Research Electronics Division, Code: 312 Ballston Tower One 800 N. Quincy Street Arlington, VA 22217-5660	3
Administrative Contracting Officer Office of Naval Research Regional Office Atlanta 101 Marietta Tower, Suite 2805 101 Marietta Street Atlanta, GA 30323-0008	1
Director, Naval Research Laboratory ATTN: Code 2627 Washington, DC 20375	1
Defense Technical Information Center Bldg. 5, Cameron Station Alexandria, VA 22314	2